



Titanium dioxide encapsulated carbon-nitride nanosheets derived from MXene and melamine-cyanuric acid composite as a multifunctional electrocatalyst for hydrogen and oxygen evolution reaction and oxygen reduction reaction



Linghao He^{a,b,1}, Jiameng Liu^{a,1}, Yongkang Liu^a, Bingbing Cui^a, Bin Hu^{a,b}, Minghua Wang^{a,b}, Kuan Tian^{a,b}, Yingpan Song^a, Shide Wu^a, Zhihong Zhang^{a,b,*}, Zhikun Peng^{c,**}, Miao Du^{a,*}

^a Henan Provincial Key Laboratory of Surface and Interface Science, Zhengzhou University of Light Industry, Zhengzhou 450002, P. R. China

^b Henan Collaborative Innovation Center of Environmental Pollution Control and Ecological Restoration, School of Materials and Chemical Engineering, Zhengzhou University of Light Industry, Zhengzhou 450002, China

^c College of Chemistry and Molecular Engineering, Zhengzhou University, Zhengzhou 450001, China

ARTICLE INFO

Keywords:

Hydrogen evolution reaction
Oxygen evolution reaction
Oxygen reduction reaction
MXene
Carbon-nitride nanosheets

ABSTRACT

An advanced trifunctional electrocatalyst based on a series of composites composed of TiO₂-encapsulated carbon-nitride (CN_x) (denoted as TiO₂C@CN_x) is developed, which is derived from the Ti₃C₂T_x and melamine-cyanuric acid calcinated at different temperatures. Among the series of TiO₂C@CN_x nanosheets, the TiO₂C@CN_{x,950} (obtained by calcination at 950 °C) hybrid exhibits robust trifunctional electrocatalytic activity toward the hydrogen evolution reaction (HER), oxygen evolution reaction (OER), and oxygen reduction reaction (ORR) by combining the excellent electrochemical activity of the graphene-like nanostructure and the high electrocatalytic performances of TiO₂ nanoparticles. When TiO₂C@CN_{x,950} is used as the electrocatalyst for water splitting, a current density of 10 mA cm⁻² ($E_f = 10$) is achieved at a low cell voltage of 1.50 V vs. reversible hydrogen electrode. Meanwhile, the overall oxygen activity of the TiO₂C@CN_{x,950} exhibits good reversible oxygen reaction, giving a small potential difference between the $E_f = 10$ for OER and the half-wave potential for ORR (0.75 V). Moreover, a simply equipped Zn-air battery is assembled using a homemade cathode, showing open-circuit potential of 1.344 V, which also can supplied an electrical power and produced H₂ at the cathode and O₂ at the anode. Consequently, this work can pave a path for developing multifunctional electrocatalysts for water splitting and liquid Zn-air battery.

1. Introduction

Increasing demands of renewable energy generation, metal air batteries, and artificial photosynthesis have stimulated intense research on energy conversion and storage systems [1]. Therefore, development of efficient electrocatalysts for the oxygen evolution reaction (OER), hydrogen evolution reaction (HER), and oxygen reduction reaction (ORR) has been the focus of much recent attention due to the rapidly increasing importance of electrochemical energy applications. Although an abundance of electrocatalysts with excellent performance has been found and designed for applications in the area of

electrocatalysis, most of them simply possess a single functional property, which can hardly satisfy the needs for the development of sustainable energy systems. In practical applications, the bifunctional catalyst toward HER/OER is required in a water splitting cell, as well as OER/ORR in metal-air batteries and unitized regenerative fuel cells. Therefore, a trifunctional catalyst (HER/OER/ORR) would be explored for highly efficiently self-powered water splitting [2]. Searching for electrocatalysts with multifunctional characteristics that can be applied to various fields, such as HER, OER and ORR, seems to be the future trend [3]. To date, these electrode reactions generally need to be catalyzed by precious metals, such as platinum (Pt), iridium (Ir), or

* Corresponding authors at: Henan Provincial Key Laboratory of Surface and Interface Science, Henan Collaborative Innovation Center of Environmental Pollution Control and Ecological Restoration, School of Materials and Chemical Engineering, Zhengzhou University of Light Industry, Zhengzhou 450002, China.

** Corresponding author.

E-mail addresses: mainzhh@163.com (Z. Zhang), zhikunpeng@163.com (Z. Peng), dumiao@zzuli.edu.cn (M. Du).

¹ These authors contributed equally.

ruthenium (Ru)-based oxide catalysts, to gain fast reaction kinetics for commercial applications [4,5]. However, these precious metal-based electrocatalysts are expensive and available only in limited reserves, leading to the limitations of their applications in relevant clean-energy technologies [6]. Although many efforts have been provided on developing transition metal-based catalysts, a number of challenges still exist, such as high costs, poor durability, and their susceptibility to gas poisoning and negative environmental effects. Among the different transition metal catalysts, transition metal–nitrogen–carbon (M–N–C, M = Fe, and Co) complex has been recognized as one of the most promising alternatives for HER, OER, and ORR due to their low cost and facile preparation [7]. Howbeit, most M–N–C catalysts were derived from corresponding precursors by pyrolysis at high temperature, wherein the pyrolysis generates not only catalytically active M–N_x sites but also inactive metal nanoparticles due to the aggregation of metal species during the pyrolysis, leading to decreasing the electrode catalyst activity [8,9]. Therefore, to precisely design pyrolysis precursor that can preferentially generate other catalysts with comprehensive and efficient catalytic performances is highly desirable.

The family of two-dimensional (2D) materials has been enriched by a new but potentially huge group of early transition metal carbides/carbonitrides known as MXenes (e.g., Ti₃C₂, Ti₂C, Nb₂C, V₂C, Ti₃CN, and Mo₂C) with unique structure and electronic properties. MXenes have been employed successfully in a wide variety of electrochemical applications including supercapacitors [10], Li and multivalent ion batteries [11], and as electrocatalysts [12] due to their high electronic conductivity and hydrophilic nature. For example, computational screening study of 2D-layered M₂XT_x (M = metal; X = (C, N); and T_x = surface functional groups) predicted that Mo₂CT_x can be used as an active catalyst candidate for the HER [12]. Hierarchical “nanoroll” like MoS₂/Ti₃C₂T_x hybrid was fabricated by combining liquid nitrogen-freezing and subsequent annealing, exhibiting excellent HER catalytic activity [13]. New MXene–Ag composites exhibited unexpected electrocatalytic activity for the ORR [14]. For energy-related applications, the exploitation of MXenes may bring additional benefit to volumetric energy density because of their much higher densities than that of graphene as both the active and/or matrix materials [5]. Recently, treatment of layered Ti₃C₂T_x at elevated temperatures in air or flowing CO₂ results in the formation of anatase TiO₂ embedded in amorphous carbon sheets [15,16]. Notably, the defective structure containing TiO₂ was reported to be an efficient catalyst for ORR despite the necessity to combine this material with carbon nanoparticles to improve the overall material conductivity [17]. This method has been reported as efficient ways to alter the surface chemistry to enhance the electrochemical properties of MXenes. For instance, Naguib et al. reported that flash oxidation of 2D Ti₃C₂ in air at 1150 °C for 30 s formed TiO₂/C composite, and the resulting material showed extremely high cycling rates when it was tested as anode in Li-ion batteries [15]. Rakhi et al. reported that annealing Ti₂CT_x (T stands for surface terminating functional groups) in inert atmospheres (Ar, N₂, and N₂/H₂) significantly improved its supercapacitor performance [18]. Considering the excellent photocatalytic activity of the TiO₂ nanoparticles, the obtained TiO₂@C derived from Ti₂CT_x MXene was often exploited as the photocatalysts for hydrogen evolution [19]. As the electrocatalyst, however, the Ti₃C₂T_x MXene normally was combined with other components, exhibiting the excellent OER [20] or HER performances [13]. Clearly, the development of MXene-based synergistic hybrid system is still in its very infant stage in contrast to the prosperity of other 2D materials. Their properties are still poorly understood, and numerous potentials are largely unexploited. Consequently, to investigate the electrocatalytic activity of the MXene-based nanomaterials is highly desirable due to their low cost, mass production, and feasible post synthesis.

Besides, metal-free catalysts, such as graphene, carbon nanotubes or carbon nanosheets, carbon nitride, and boron nitride, have attracted worldwide attention due to low cost, abundant reserves and excellent

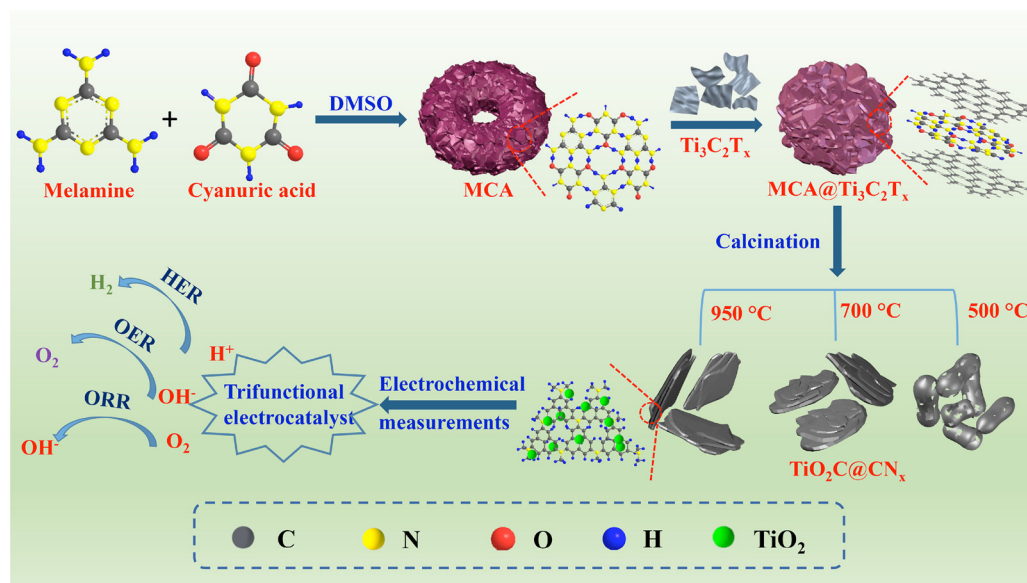
catalytic properties [21]. Among them, the graphitic carbon nitride-based composites are considered as promising candidates for the energy and catalytic fields owing to facile preparation, special layer structure, and excellent chemical stability [22]. Wang et al. reported that the NiSe₂/graphitic carbon nitride composite exhibited favorable electrocatalytic performances toward OER with low overpotential of 290 mV at current density of 40 mA cm⁻² and low onset potential of 1.38 V [23]. Normally, graphitic carbon nitride was commonly derived from nitrogen-rich precursors by simple pyrolysis method, such as urea, melamine, and dicyandiamide [24]. Moreover, hydrogen-bonded supramolecules self-assembled by intermolecular hydrogen bonds among molecules have emerged as perfect candidates as N source precursor for N doping by simple calcination process and self-sacrificial template to manufacture porous structure [25]. Guo et al. reported the high-quality graphitic carbon nitride with reduced structural defects by judiciously combining the implementation of melamine-cyanuric acid (MCA) supramolecular aggregates and microwave-assisted thermolysis [26]. The prepared graphitic carbon nitride material can effectively generate H₂ under visible-light irradiation and the highest H₂ evolution rate achieved was 40.5 mmol h⁻¹. Sun et al. investigated the advantages of MCA supramolecular aggregates as the precursors for well-organized carbon nitride with controllable chemical and photophysical properties [27]. Zhao et al. fabricated 3D porous N-doped graphene aerogel (NGA) with GO as building block, and MCA supramolecule as both N source and self-sacrificial pore former, which exhibited excellent ORR performance in terms of positive half-wave potential and efficient methanol electrooxidation reaction [25]. Notably, the above electrocatalysts only exhibited monofunctional characteristics toward HER, ORR, or OER. Thereby, developing low cost, earth-abundant trifunctional electrocatalysts to promote the ORR, OER, and HER simultaneously under the same pH environment is highly urgent.

Considering the advantage of MXene as the excellent electrocatalyst and the potentially good OER or ORR activities of MCA, we designed and synthesized a new class of electrocatalysts simultaneously toward HER/OER/ORR reactions by compounding Ti₃C₂T_x MXene nanosheets and MCA (represented by MCA@Ti₃C₂T_x) for the first time, further calcinated into the TiO₂C@CN_x nanosheets at differently high temperatures (500, 700, and 950 °C) (Scheme 1). Combining efficient pathways for electron and electrolyte/reactant transports with the abundant accessible active sites, the TiO₂C@CN_x nanosheets calcinated at 950 °C (represented by TiO₂C@CN_{x,950}) exhibited robust and highly efficient multifunctional electrocatalytic activities toward HER, OER, and ORR, together with long-term stability in alkaline electrolyte (0.1 M KOH). The TiO₂C@CN_{x,950} only required a small overpotential (-254.5 mV) at the potential of 10 mV cm⁻² for HER in 0.1 M KOH comparable with most metal oxide catalyst and also exhibited a comparable OER activity to RuO₂ nanoparticles with a reasonably good ORR activity. The as-fabricated TiO₂C@CN_{x,950} catalyst further demonstrated excellent water splitting activity as the OER/HER and good OER/ORR bifunctional catalysts. This study opens a new avenue for the development of low-cost carbon-based catalysts to replace noble metals for a large variety of applications, ranging from fuel cells through metal-air batteries to water splitting devices. Our work establishes a facile strategy for the preparation of the TiO₂C@CN_x hybrid and an efficient and stable trifunctional electrocatalyst for overall water splitting and Zn-air batteries. This strategy can be extended to fabricate other nanomaterials for energy fields.

2. Experimental section

2.1. Chemicals and reagents

Melamine and cyanuric acid were purchased from Aladdin Reagent Co. Ltd. (Shanghai, China). Dimethyl sulfoxide (DMSO) and HF were purchased from Solarbio Life Sciences Reagent Co. Ltd. (Beijing, China). Ti₃C₂T_x were ordered from HAOXI Research Nanomaterials, Inc. Co.



Ltd. (Shanghai, China). All of the chemicals used were of analytical reagent grade and used without further purification. Milli-Q water ($> 18.2 \Omega \text{ cm}$) was used throughout this study.

2.2. Preparation of the $\text{Ti}_3\text{C}_2\text{T}_x$ nanosheets

Typically, 10 g Ti_3SiC_2 MXene phase was immersed in 100 mL of 45% concentrated HF solution at room temperature for 12 h to extract Si. The resulting suspension was centrifuged and washed using deionized water thrice to obtain the multilayer $\text{Ti}_3\text{C}_2\text{T}_x$ powder. To obtain few-layer $\text{Ti}_3\text{C}_2\text{T}_x$, multilayered $\text{Ti}_3\text{C}_2\text{T}_x$ was immersed in DMSO for 24 h at room temperature, centrifuged and washed with deionized water for several times, and dispersed in 200 mL of deionized water. Subsequently, the suspension was stripped by ultrasonic cell disruptor for 4 h and centrifuged for 30 min at 3500 rpm. After filtering, the supernatant was freeze-dried for 24 h to obtain the few-layer $\text{Ti}_3\text{C}_2\text{T}_x$.

2.3. Synthesis of MCA and $\text{MCA}@\text{Ti}_3\text{C}_2\text{T}_x$ nanosheets

We synthesized MCA nanosheets according to the literature [26]. Melamine (0.5 g) and cyanuric acid (0.5 g) were dissolved in 20 and 10 mL DMSO, respectively. The solutions of melamine and cyanuric acid were then mixed together under vigorous stirring for 30 min. The white precipitation was washed with ethanol repeatedly for several times and then dried at 60 °C.

For the preparation of $\text{MCA}@\text{Ti}_3\text{C}_2\text{T}_x$ nanosheets, 0.5 g melamine was dissolved in 20 mL of DMSO. Then, 0.05 g $\text{Ti}_3\text{C}_2\text{T}_x$ was added to the above mixture and dispersed by stirring. Subsequently, a solution of cyanuric acid (0.5 g) in 10 mL of DMSO was added under the vigorous stirring for 30 min. The gray precipitation was washed with ethanol repeatedly for several times and then dried at 60 °C in an oven to yield $\text{MCA}@\text{Ti}_3\text{C}_2\text{T}_x$ composite.

2.4. Synthesis of CN_x , $\text{TiO}_2@\text{C}$, and the series of $\text{TiO}_2\text{C}@\text{CN}_x$ nanosheets

The as-prepared $\text{MCA}@\text{Ti}_3\text{C}_2\text{T}_x$ composite was placed in a furnace and heat-treated under an Ar flow at 500 °C, 700 °C, and 950 °C for 1 h at a heating rate of 5 °C min⁻¹, separately. Accordingly, the $\text{TiO}_2\text{C}@\text{CN}_{x,500}$, $\text{TiO}_2\text{C}@\text{CN}_{x,700}$, and $\text{TiO}_2\text{C}@\text{CN}_{x,950}$ were obtained. For comparison, MCA and $\text{Ti}_3\text{C}_2\text{T}_x$ were also heat-treated under an Ar flow at 950 °C for 1 h at a heating rate of 5 °C min⁻¹ to obtain CN_x and $\text{TiO}_2@\text{C}$, respectively.

Scheme 1. Schematic illustration of the preparation of the series of $\text{TiO}_2\text{C}@\text{CN}_x$ nanosheets as trifunctional electrocatalysts toward HER, OER, and ORR, including (i) the preparation of MCA and $\text{MCA}@\text{Ti}_3\text{C}_2\text{T}_x$ nanosheets, (ii) the calcination of $\text{Ti}_3\text{C}_2\text{T}_x$, MCA, and $\text{MCA}@\text{Ti}_3\text{C}_2\text{T}_x$ nanosheets, and (iii) the investigation of the developed electrocatalysts.

2.5. Characterizations

X-ray diffraction (XRD) measurements were recorded on a Rigaku D/Max-2500 X-ray diffractometer using Cu K α as a radiation. The corresponding intensity data were collected in the step-scan mode with a scan rate of 5° min⁻¹ and a step size of 0.02°. Raman spectra were obtained on a Renishaw inVia Raman spectrometer with a solid-state laser (excitation at 532 nm) at room temperature in the range of 50–4000 cm⁻¹. Fourier transform infrared spectroscopy (FT-IR) was performed by using a Bruker TENSOR27 spectrometer (32 scans at 4 cm⁻¹ resolution). X-ray photoelectron spectroscopy (XPS) analysis was conducted using a Thermo Fisher ESCALAB 250Xi spectrometer equipped with an Al anode (Al-K α 1486.6 eV). Field emission scanning electron microscopy (FE-SEM) was conducted using a JSM-6490LV scanning electron microscope. Surface morphology was determined by using high-resolution transmission electron microscopy (TEM, JEOL JEM-2100) with a field emission gun of 200 kV, respectively. Determination of specific surface area of samples were carried out by Brunauer-Emmett-Teller (BET) methods using a Micromeritics ASAP2022 instrument at the temperature of liquid nitrogen. Prior to measurement, all of the samples were degassed at 573 K for 8 h.

2.6. Electrochemical measurements

HER tests were performed in a conventional three-electrode system at an electrochemical station (CHI660E, Shanghai Chenhua Instruments Co., China), using Ag/AgCl (3.5 M KCl solution) electrode as the reference electrode, Pt wire as the counter electrode and glass carbon electrode (GCE) of 3 mm in diameter as the working electrode. Linear sweep voltammetry (LSV) with scan rate of 5 mV s⁻¹ was measured in 0.5 M H₂SO₄ deaerated with Ar at room temperature for 30 min. To prepare the working electrode, 1.0 mg catalyst and 100 μ L of Nafion (DuPont, 5 wt %) were dispersed in 900 μ L of water by sonication, thereby forming a homogeneous catalyst ink. The obtained suspension (10 μ L) was loaded onto the GCE and dried naturally at room temperature. The final loading for all catalysts and commercial Pt/C electrocatalysts on the GCE is about 0.283 mg cm⁻². The potential of Ag/AgCl electrode was calibrated with respect to a reversible hydrogen electrode (RHE). The calibration was performed in the high purity hydrogen saturated electrolyte with Pt mesh as the counter electrode. The electrochemical impedance spectroscopy (EIS) was carried out in the same configuration when the working electrode was biased at the overpotential of −240 mV from 10⁵ Hz to 10^{−2} Hz with an amplitude

of 5 mV. Chronoamperometric measurement (the potential (η) = -250 mV) was performed to evaluate the long-term stability.

OER tests were conducted in a three-electrode with a rotating disk electrode (RDE). A Pt wire and a 3.5 M Ag/AgCl electrode were used as the counter electrode and reference electrode, respectively. The catalyst-modified glass carbon RDE was used as the working electrode with a rotating speed of 1600 rpm. LSV with scan rate of 5 mV s⁻¹ was measured in 0.1 M KOH. All measured potentials vs. Ag/AgCl were converted to RHE scale based on the Nernst equation below: $E_{\text{RHE}} = E_{\text{Ag/AgCl}} + 0.0591 \times \text{pH} + E^{\theta}_{\text{Ag/AgCl}}$, where E_{RHE} is the applied potential vs. RHE; $E_{\text{Ag/AgCl}}$ is the applied potential vs. Ag/AgCl reference electrode, and $E^{\theta}_{\text{Ag/AgCl}}$ is the standard potential of the Ag/AgCl reference electrode. In 0.5 M H₂SO₄, $E_{\text{RHE}} = E_{\text{Ag/AgCl}} + 0.22$ V. In 0.1 M KOH, $E_{\text{RHE}} = E_{\text{Ag/AgCl}} + 0.915$ V.

ORR tests were measured in an O₂-saturated solution, a Pt wire was used as the counter electrode, a 3.5 M Ag/AgCl electrode as the reference electrode, and the catalyst-modified glass carbon RDE as the working electrode with a rotating speed of 1600 rpm. LSV with a scan rate of 5 mV s⁻¹ was measured in 0.1 M KOH. A flow of O₂ was maintained over the electrolyte during the recording of cyclic voltammetry (CV) in order to ensure its continued O₂ saturation. In control experiments, CV measurements were also performed in nitrogen atmosphere by switching to N₂ flow through the electrochemical cell.

Overall water splitting electrocatalysis was examined by polarization curves using a two-electrode system in 1.0 M KOH at a scan rate of 5 mV s⁻¹. The TiO₂C@CN_x loaded on Ni foam was used as both the positive and negative electrodes. The long-term durability tests were performed using chronoamperometric measurements. All polarization curves presented were *iR*-corrected.

2.7. Aqueous Zn-air batteries assembly

The liquid Zn-air battery was assembled using the homemade cathode. The electrocatalyst ink was dropped onto a carbon cloth with a loading of 1.0 mg cm⁻² and dried at room temperature, which was used as the air cathode. A polished Zn plate washed with 5% HCl and deionized water was used as the anode, and 6.0 M KOH with 0.2 M zinc acetate (ZnAC) was used as the electrolyte for Zn-air batteries. Battery performance was conducted on the electrochemical workstation.

3. Results and discussion

3.1. Crystal and chemical structures of all samples

For comparison, MCA and Ti₃C₂T_x were also heat-treated at 950 °C under the same condition with TiO₂C@CN_{x,950}, denoted as CN_x and TiO₂@C, respectively. The FT-IR, XRD patterns, and Raman spectra of MCA and CN_x nanosheets were characterized and summarized in Fig. S1. These spectra of Ti₃C₂T_x and TiO₂@C nanosheets are displayed in Fig. S2. The related discussions are also given in S1 and S2 sections of the Supporting information. This condition hints the formation of the chemical structure of MCA nanosheets, and the graphene-like structure is obtained for the CN_x nanosheets. The rich functional groups, such as C=O, C—O, C—O, —NH, and Ti—O—Ti, are present in the Ti₃C₂T_x nanosheets, leading to the formation of TiO₂ nanoparticles embedded in the carbon substrate after calcination at 950 °C, i.e., TiO₂@C.

Furthermore, the FT-IR, XRD patterns, and Raman spectra of MCA@Ti₃C₂T_x and the series of TiO₂C@CN_x composites are investigated and displayed in Fig. 1, showing that these characterizations of MCA@Ti₃C₂T_x are similar to those of the pristine MCA (curve i, Fig. S1). This condition suggests the MCA coverage onto the surface of Ti₃C₂T_x nanosheets. With regard to the FT-IR spectrum of the TiO₂C@CN_{x,500} composite (curve ii, Fig. 1a), clearly, the characteristic peaks of the MCA precursors disappear, and the new peaks emerge at 810, 1240, 1318, 1411, 1460, 1568, and 1640 cm⁻¹ belonging to the stretching vibrations of the CN_x heterocycles, signifying the formation

of tris-triazine [28]. In TiO₂C@CN_{x,700} and TiO₂C@CN_{x,950} composites (curves iii and iv, Fig. 1a), their FT-IR spectra show that the characteristic peaks of CN_x disappear, together with the peaks similar to those of TiO₂@C. This phenomenon hints the close chemical structure of these two samples to that of the TiO₂@C nanosheets.

As displayed in Fig. 1b, the XRD pattern of MCA@Ti₃C₂T_x presents two main peaks at 2θ = 10° and 28° (curve i, Fig. 1b). This XRD pattern shows similar characteristic peaks to that of MCA [26], attributed to the periodic arrays of intraplanar stacking and interlayer aromatic stacking of MCA. As for the series of TiO₂C@CN_x nanosheets (curves ii, iii, and iv, Fig. 1b), the XRD patterns are close to that of the TiO₂@C nanosheets composed of anatase and rutile TiO₂, indicating their similar crystal structure. As illustrated in Fig. 1c, the Raman spectrum of MCA@Ti₃C₂T_x is similar to that of MCA (curve i). The most intense peak at 693 cm⁻¹ is ascribed to the ring breathing II mode and involves in-plane deformation of the triazine ring [29]. With regard to the Raman spectra of series of TiO₂C@CN_x composites, peaks are observed similar to that of the TiO₂@C nanosheets but with different I_D/I_G values, i.e., 0.7, 0.43, and 0.31 for TiO₂C@CN_{x,500}, TiO₂C@CN_{x,700}, and TiO₂C@CN_{x,950}, respectively. This result demonstrates that the intensities of defect nanostructures decrease with the increase of the calcination temperature, whereas the graphene structure content increases [30]. Additionally, the N₂ adsorption-desorption isotherms of MCA@Ti₃C₂T_x and the series of TiO₂C@CN_x composites are measured and displayed in Fig. 1d. This phenomenon shows the specific surface areas of MCA@Ti₃C₂T_x, TiO₂C@CN_{x,500}, TiO₂C@CN_{x,700}, and TiO₂C@CN_{x,950} composites of 16.97, 44.56, 15.35, and 11.57 cm² g⁻¹, respectively. This condition illustrates that the calcination at high temperature results in the decrease of the specific surface of the TiO₂C@CN_x nanosheets.

The chemical structures of all samples are also investigated by XPS. The XPS survey spectra of all samples are depicted in Fig. S3, wherein the O 1s (532 eV), C 1s (284.8 eV), and N 1s (397.7 eV) signals are observed, and the Ti 2p (460 eV) is also obtained in Ti₃C₂T_x, TiO₂@C, and the series of TiO₂C@CN_x composites in all samples. Concurrently, the corresponding atomic% of each containing element is summarized in Table S1. The related detailed description is supplied in S3 section (Supporting information). To understand the chemical environment and component variation of the samples before and after the calcination, the core-level XPS spectra of all elements containing MCA and its derivative, Ti₃C₂T_x and its derivation, and MCA@Ti₃C₂T_x and the series of derivatives were analyzed by XPSPEAK1 software. The detailed description of C 1s, N 1s, and O 1s core-level XPS spectra deconvolutions of MCA and CN_x are supplied in Fig. S4. We can conclude from the core-level XPS analysis that the decomposition of the carbon-related groups at high temperature forms rich C=C groups and π—π* binding. This phenomenon means that decomposition of the carbon-related groups at high temperature forms the unsaturated bonds, together with the oxidation of the nitrogen group. The coexistence of large amounts of the C=C groups and π—π* suggests the highly conjugated chemical structure of CN_x which can boost the electrocatalytic activity due to this structure transformation [31,32]. From the core-level XPS of C 1s, Ti 2p, and O 1s containing the Ti₃C₂T_x and TiO₂@C nanosheets (Fig. S5), the calcination at high temperature has no substantial effect on the chemical structure and component.

As displayed in Fig. 2, the C 1s, N 1s, and O 1s core-level XPS spectra of the MCA@Ti₃C₂T_x nanosheets and the series of the calcinated TiO₂C@CN_x nanosheets are analyzed. This phenomenon shows the similar deconvoluted results of the obtained C 1s and N 1s core-level XPS spectra of the MCA@Ti₃C₂T_x nanosheets to those of the bulk MCA (Fig. 2a1 and a2). Only two peaks representing the C=O and C—O groups remained for the composite in the O 1s core-level XPS spectrum (Fig. 2a3). All these findings are due to the coverage of the MCA layer onto the Ti₃C₂T_x nanosheets surface, which prevents the Ti₃C₂T_x nanosheets to be determined by XPS. When MCA@Ti₃C₂T_x nanosheets are calcinated at 500 °C, one strong peak at 288.3 eV (N—C = O) presents in

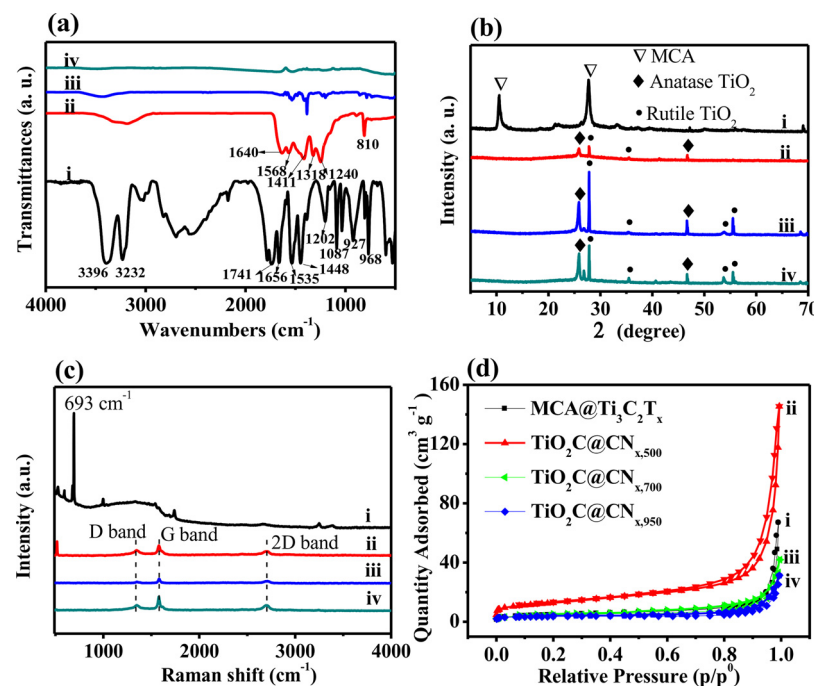


Fig. 1. (a) FT-IR, (b) XRD patterns, (c) Raman spectra and (d) Nitrogen adsorption-desorption isotherms of (i) MCA@Ti₃C₂T_x, (ii) TiO₂C@CN_{x,500}, (iii) TiO₂C@CN_{x,700}, and (iv) TiO₂C@CN_{x,950} composites.

the TiO₂C@CN_{x,500}, together with a weak peak at 284.8 eV (C–C) (Fig. 2b1). The disappearance of the C=O and $\pi-\pi^*$ groups and the low N 1s intensity signify that they are oxidized and decomposed to the small molecules, which escape from the matrix [33]. This result is also confirmed by a new peak at 404.8 eV originated from the N 1s core-level XPS spectrum (Fig. 2b2) due to the oxidized nitrogen ($-NO_x$) [34]. As for the O 1s core-level XPS spectrum of the TiO₂C@CN_{x,500} nanocomposite (Fig. 2b3), the high binding energy at 533.2 eV represents the adsorbed oxygen. In TiO₂C@CN_{x,700} and TiO₂C@CN_{x,950} composites, nevertheless, similar results for the high resolution of C 1s XPS spectra are observed, which is also similar to that of the TiO₂@C nanosheets. As aforementioned, the MCA layer can be transferred to the carbon nitride compound, in which the chemical structure is similar to the graphene oxide. Consequently, the TiO₂C@CN_x obtained by calcining at a very high temperature is close to the TiO₂-doped graphene composite. Nevertheless, two more peaks at 529.5 and 530.2 eV are found in their O 1s core-level XPS spectra, corresponding to Ti–O and O vacancies, respectively. Simultaneously, the Ti 2p core-level XPS spectra of MCA@Ti₃C₂T_x and the series of TiO₂C@CN_x composites are simulated and illustrated in Fig. S6. As expected, no substantial signal of Ti 2p is maintained in the MCA@Ti₃C₂T_x and TiO₂C@CN_{x,500} nanosheets due to the coverage of the thick MCA and CN_x layer, separately.

Howbeit, complicated Ti 2p core-level XPS spectra of TiO₂C@CN_{x,700} and TiO₂C@CN_{x,950} composites are observed, wherein the newly deconvoluted peaks at 457.3 and 462.5 eV are ascribed to the Ti 2p_{3/2} and Ti 2p_{1/2} of Ti³⁺ defects, respectively. This observation is consistent with the reported literature [35]. Given that Ti³⁺ species on the composite surface are known to be unstable and easily oxidize upon calcination, the synthesis of stable Ti³⁺-doped TiO₂ remains challenging. In TiO₂C@CN_x composites, however, Ti³⁺ species are believed to be stabilized upon hybridization with graphene-like CN_x. As reported by Boppella et al., the presence of Ti³⁺ sites is believed to increase the electron density, further strengthening the electrocatalytic activity toward ORR [36]. Compared with the TiO₂C@CN_{x,700}, the relative content of the Ti³⁺ species containing TiO₂C@CN_{x,950} is much higher mainly due to the high stabilization ability of the graphene structure formed in the TiO₂C@CN_{x,950} toward the Ti³⁺ species. This finding also

suggests the excellent electrocatalytic performance. These results indicate that the formed TiO₂C@CN_x composite prepared under the high temperature is composed of the rich and usual valence states of Ti (Ti⁴⁺ and Ti³⁺) and graphene-like structured carbon doped with nitrogen, carbonyl group, and hydroxyl group.

3.2. Surface morphologies of all samples

The surface nanostructure of all samples was characterized by SEM and TEM. As shown in Fig. S7, the pristine MCA sample displays porous sphere-like morphology (Figs. S7a and S7b), whereas the CN_x nanosheets are composed of irregular nanoparticles (Figs. S7c and S7d), suggesting that the MCA nanospheres collapsed after the pyrolysis. This phenomenon is mainly caused by the large amount of gases, such as CO, CO₂, NO, NO₂, or H₂O spontaneously generated during the polymerization of the MCA supermolecular aggregates [33,37]. TEM images of MCA further prove that sphere-like nanostructure is aggregated by the multilayered nanosheets (Fig. S8a), whereas the high-resolution TEM (HR-TEM) of MCA shows that the entire sample consists of very thin nanosheets (Fig. S8b). TEM image of CN_x nanosheets display that CN_x is composed of highly ultrathin-layered nanosheets with wrinkled surface (Fig. S8c). A close observation by HR-TEM in Fig. S8d shows that the entire sample consists of crystalline and amorphous domains. This condition illustrates the lattice space of 0.34 nm in the crystalline domain (Fig. S8d), consistent with (002) plane of graphitic carbon. As shown in Figs. S9a and S9b, the exfoliated Ti₃C₂T_x nanosheets are composed of the irregular nanosheets, indicating that the stacked Ti₃C₂T_x is separated under the high-powered ultrasonication. As can be seen from the TEM images (Figs. S10a and 10b), the clear exfoliation of flaky structure is observed. High crystallinity of Ti₃C₂T_x sheets is evident from TEM at a lattice spacing of approximately 0.33 nm, corresponding to the (110) planes of the rutile TiO₂ originated from the local heat generated during HF treatment of the MXene phase [18]. With regard to the TiO₂@C nanosheets, no substantial change is observed from SEM (Figs. S9c and S9d) and TEM images (Fig. S10c), whereas the HR-TEM image (Fig. S10d) clearly shows the lattice fringe at a lattice spacing of 0.35 nm. This finding is in good agreement with the (101) plane of anatase TiO₂ (JCPDS no. 21-1272). The selected area

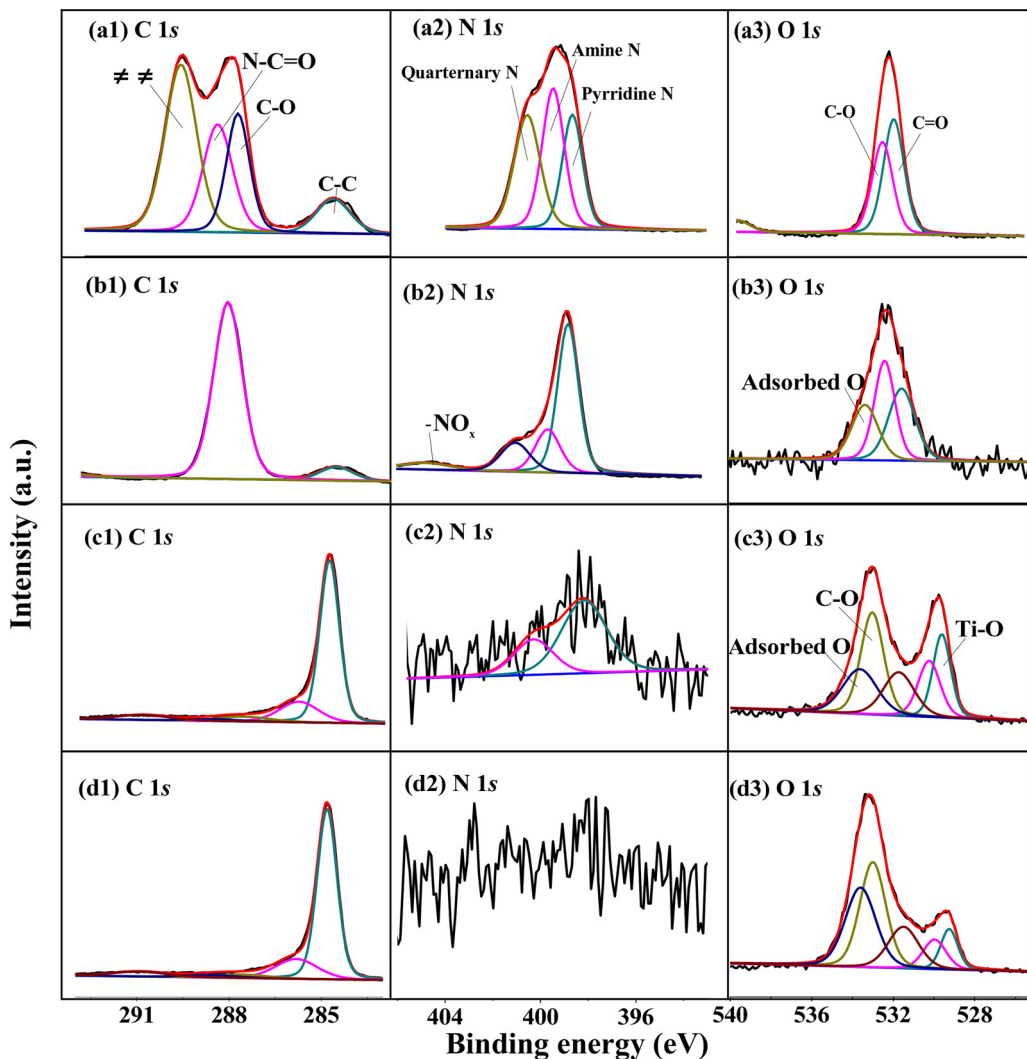


Fig. 2. C 1s, N 1s, and O 1s core-level XPS spectra of (a) MCA@ $\text{Ti}_3\text{C}_2\text{T}_x$, (b) $\text{TiO}_2\text{C}@\text{CN}_{\text{x},500}$, (c) $\text{TiO}_2\text{C}@\text{CN}_{\text{x},700}$, and (d) $\text{TiO}_2\text{C}@\text{CN}_{\text{x},950}$ composites.

electron diffraction (SAED) of $\text{TiO}_2@\text{C}$ (the inset of Fig. S10d) exhibits several bright rings made up of discrete spots, which can be indexed to the (301), (200), (112), (321), and (224) planes of TiO_2 . This result suggests the high crystallinity of $\text{TiO}_2@\text{C}$ caused by high temperature calcination.

When MCA is combined with $\text{Ti}_3\text{C}_2\text{T}_x$ nanosheets (Fig. 3a), i.e., MCA@ $\text{Ti}_3\text{C}_2\text{T}_x$, the irregular nanospheres with uniform size are observed attributed to the MCA coverage around the $\text{Ti}_3\text{C}_2\text{T}_x$ nanosheets. Moreover, the TEM images of MCA@ $\text{Ti}_3\text{C}_2\text{T}_x$ reveal its similar nanostucture to that of the MCA (Fig. 4a), along with the multiple pore and amorphous structure (Fig. 4b). In $\text{TiO}_2\text{C}@\text{CN}_{\text{x},500}$ (Fig. 3b), the sphere-like structure completely collapsed due to the large amount of gases, such as NH_3 , CO , or CO_2 [33,37], spontaneously generated during the calcination at 500 °C. The quick escape of gases forms highly fluffy and porous structures. The TEM image of $\text{TiO}_2\text{C}@\text{CN}_{\text{x},500}$ composite (Fig. 4c) also reveals that the multiple layers are overlapped together with the porous structure. Besides the amorphous carbon structure, the high crystallinity of $\text{TiO}_2\text{C}@\text{CN}_{\text{x},500}$ is observed (Fig. 4d), indicating the pyrolysis of the outer layer of MCA. For the $\text{TiO}_2\text{C}@\text{CN}_{\text{x},700}$ nanosheets (Fig. 3c), however, the cotton-like nanosheets disappear, only leaving the irregular nanosheets. As displayed in their TEM image (Fig. 4e), the irregular-shaped nanosheets appear, whereas the layers increases the transparency of the nanosheets moving toward the dark shade. According to the HR-TEM image (Fig. 4f), the nucleation and growth of TiO_2 are clearly identified on the Ti_3C_2 surface. However, the SEM

image of $\text{TiO}_2\text{C}@\text{CN}_{\text{x},950}$ (Fig. 3d) reveals that the thin layers combine closely with each other, showing relatively small size. As displayed in Fig. 4g, the nucleation and growth of ultrasmall nanoparticles are clearly identified. Considering the previous characterization results, the ultrasmall nanoparticles on the surface of the graphene-like nanosheets were TiO_2 nanoparticles. Meanwhile, clear inter-lattice spacings of 0.35 nm assigned to the (101) plane of anatase TiO_2 are observed in the HR-TEM image of $\text{TiO}_2\text{C}@\text{CN}_{\text{x},950}$ (Fig. 4h). From the SAED of the series of $\text{TiO}_2@\text{C}$ (the insets of Fig. 4d, f, and h), we can find some other planes of TiO_2 except of the (101) plane, such as (211), (200), and (301), which change with the calcination temperature. Compared with the other $\text{TiO}_2@\text{C}$ nanosheets, the coexistence of TiO_2 and Ti_2O_3 nanoparticles in the $\text{TiO}_2\text{C}@\text{CN}_{\text{x},950}$ nanosheets indicates that the CN_{x} presence can facilitate the reduction of Ti^{4+} to Ti^{3+} , consistent with the results of XRD, XPS, and Raman spectroscopy. As reported in literatures, TiO_2 nanoparticles can enhance the electrocatalytic activity of $\text{TiO}_2\text{C}@\text{CN}_{\text{x},950}$ because its Ti^{3+} species can increase the electron density [36]. In addition, to better understand the uniformity of MAC and $\text{Ti}_3\text{C}_2\text{T}_x$, a simple mixing sample of MCA and $\text{Ti}_3\text{C}_2\text{T}_x$ was prepared by grinding in order to compare the MCA@ $\text{Ti}_3\text{C}_2\text{T}_x$ composite obtained by one-step method. The physical-mixture was denoted as MCA/ $\text{Ti}_3\text{C}_2\text{T}_x$. Since the physically mixed sample only was calcined at 950 °C, it was labeled as $\text{TiO}_2\text{C}@\text{CN}_{\text{x},950}$. As shown in Fig. S11, compared to the uniform and irregular nanospheres of the MCA@ $\text{Ti}_3\text{C}_2\text{T}_x$ composite that is almost identical to morphology of MCA, the physical-mixture MCA/

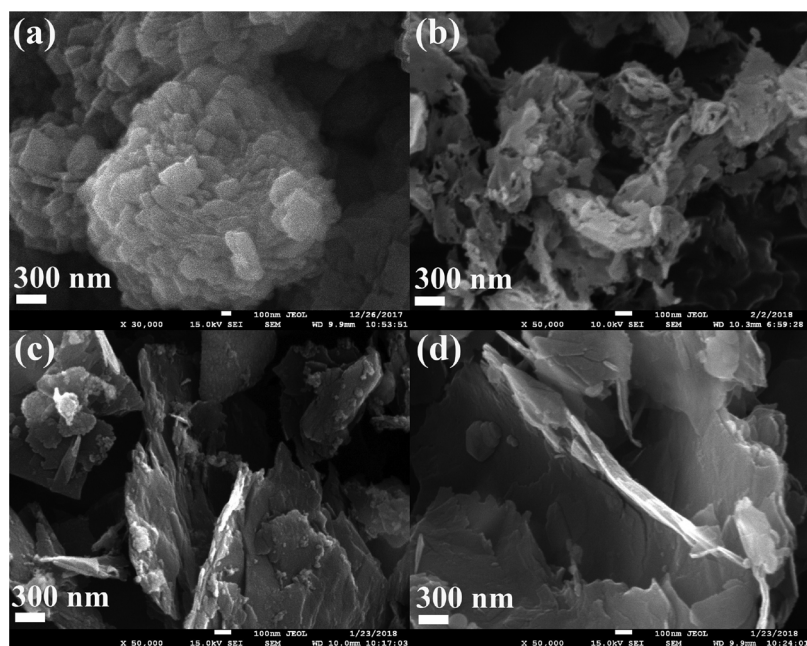


Fig. 3. Low- and high-magnitude SEM images of (a) MCA@ $\text{Ti}_3\text{C}_2\text{T}_x$, (b) $\text{TiO}_2\text{C}@\text{CN}_{\text{x},500}$, (c) $\text{TiO}_2\text{C}@\text{CN}_{\text{x},700}$, and (d) $\text{TiO}_2\text{C}@\text{CN}_{\text{x},950}$ composites.

$\text{Ti}_3\text{C}_2\text{T}_x$ presents stacked irregular blocks and scattered particles. After calcination, compared to the uniform dispersion of $\text{TiO}_2\text{C}@\text{CN}_{\text{x},950}$ nanosheets, the $\text{TiO}_2\text{C}@\text{CN}_{\text{x},950}$ nanosheets appear to be thicker. It indicates that the $\text{Ti}_3\text{C}_2\text{T}_x$ nanosheets cannot be well combined with the MCA only by physically mixing.

3.3. ORR electrocatalytic performances of all samples

Based on the XRD, FT-IR, XPS, Raman, SEM, and TEM results, we have realized the successful coupling of $\text{TiO}_2@\text{C}$ and CN_{x} . Their combination leads to the obvious interaction between Ti, C, and graphene-like CN_{x} during calcination treatment. As a result, $\text{TiO}_2\text{C}@\text{CN}_{\text{x}}$ is expected to exhibit pore structure and large electrochemical active surface area (ECSA). Besides, the combination of defective TiO_2 with carbon nitride forms an effective transport channel and then improves the electron transfer efficiency to acquire ideal electrochemical performance [38,39]. Thus, $\text{TiO}_2\text{C}@\text{CN}_{\text{x}}$ nanosheets have enormous potentiality to become a highly active catalyst for HER, OER, and ORR.

ORR plays an important role in regulating the performance of fuel cells or chlor-alkali electrolyzer. However, the development of ORR electrocatalysts with high activity at low cost still remains a great challenge. Recent studies have demonstrated the potential to use metal-free or nonprecious metal electrocatalysts to replace Pt-based electrodes in fuel cells. To investigate the ORR performances of the series of $\text{TiO}_2\text{C}@\text{CN}_{\text{x}}$ catalysts, RDE measurements were carried out in O_2 -saturated 0.1 M KOH. The commercial 20 wt% Pt/C was also measured for comparison. As illustrated in Fig. 5a, a characteristic oxygen reduction peak at 0.70 V (vs. RHE) is obtained for the $\text{TiO}_2\text{C}@\text{CN}_{\text{x},700}$ and $\text{TiO}_2\text{C}@\text{CN}_{\text{x},950}$ in O_2 -saturated KOH but not in N_2 -saturated electrolyte, indicating a high ORR activity for these catalysts. This result suggests that $\text{TiO}_2\text{C}@\text{CN}_{\text{x},500}$ has no ORR activity due to no substantial oxygen reduction peak.

Afterward, the ORR performances of the series of $\text{TiO}_2\text{C}@\text{CN}_{\text{x}}$ nanosheets and Pt/C were measured by LSV curves on an RDE in O_2 -saturated 0.1 M KOH solution (Fig. 5b). As anticipated, the Pt/C catalyst shows the high ORR electrocatalytic activity with an onset potential (E_0) of 0.94 V (vs. RHE), a high kinetic-limiting current density (J_k) of -6.2 mA cm^{-2} , and a half-wave potential ($E_{1/2}$) of 0.80 V. The remarkable improvement of the ORR activity is obtained for the $\text{TiO}_2\text{C}@\text{CN}_{\text{x},950}$, exhibiting improved performance with an E_0 of 0.87 V,

an $E_{1/2}$ of 0.76 V, and a high J_k of -5.0 mA cm^{-2} . Nevertheless, the MCA@ $\text{Ti}_3\text{C}_2\text{T}_x$, $\text{TiO}_2\text{C}@\text{CN}_{\text{x},500}$, and $\text{TiO}_2\text{C}@\text{CN}_{\text{x},700}$ present poor ORR performances with a low E_0 and J_k , confirming that both of them are not an excellent ORR catalyst. J_k , $E_{1/2}$, and E_0 of all samples are displayed in Table S2. For comparison, the ORR performances of MCA and $\text{Ti}_3\text{C}_2\text{T}_x$ nanosheets before and after calcinating at 950 °C were also investigated, as displayed in Figs. S12 and S13, respectively. Concurrently, their corresponding J_k , $E_{1/2}$, and E_0 values are summarized in Tables S3 and S4, indicating that both of $\text{TiO}_2@\text{C}$ nanosheets and CN_{x} nanospheres show slightly higher ORR activities than those of MCA and $\text{Ti}_3\text{C}_2\text{T}_x$ nanosheets. Compared with many previously reported carbon nitride electrocatalysts (Table S5) measured in 0.1 M KOH, the $\text{TiO}_2\text{C}@\text{CN}_{\text{x},950}$ electrocatalyst exhibits a more positive $E_{1/2}$, signifying a superior ORR performance.

To investigate the ORR pathways (i.e., electron number transferred) catalyzed by $\text{TiO}_2\text{C}@\text{CN}_{\text{x}}$ catalysts, the Koutecky-Levich ($K-L$) equation was applied [40], and the result shows how the inverse current density (j^{-1}) varies as a function of the inverse of the square root of the rotation speed ($\omega^{-1/2}$) at different potential values. Fig. 5c shows the linear $K-L$ plots at different potentials, which are derived from the polarization curves at various rotation speeds (Fig. S14). The electron transfer number (n) value of $\text{TiO}_2\text{C}@\text{CN}_{\text{x},950}$ calculated by using the $K-L$ equation is 4.1. This value is close to the theoretical value of Pt/C (4.0) (Fig. 5d), verifying a near four-electron reaction pathway of the ORR, whereas n for $\text{TiO}_2\text{C}@\text{CN}_{\text{x},500}$ at the same potential is only 3.4, suggesting the existence of a two-electron pathway. As mentioned in other literatures, pyridinic N atoms can effectively donate electron density to adjacent carbon atoms, facilitating the adsorption of O_2 molecules and reducing the energy required for cleavage of O–O bonds of dioxygen [40,41].

Furthermore, the long-term stability of $\text{TiO}_2\text{C}@\text{CN}_{\text{x},950}$ was confirmed by LSV measurements. Fig. 5e shows no substantial change of the LSV curve on a RDE in O_2 -saturated 0.1 M KOH solution of the $\text{TiO}_2\text{C}@\text{CN}_{\text{x},950}$ catalyst after the continuous 5000 times measurements. The inset of Fig. 5e shows that the current for the $\text{TiO}_2\text{C}@\text{CN}_{\text{x},950}$ catalyst after a 48 h LSV test remains unchanged under the conditions (0.7 V with a continuous flow of O_2 in 0.1 M KOH), further indicating the superb durability of the $\text{TiO}_2\text{C}@\text{CN}_{\text{x},950}$ catalyst toward the ORR. As for the Pt/C catalyst, however, high current loss of 26.2% is observed. The excellent durability of the proposed $\text{TiO}_2\text{C}@\text{CN}_{\text{x},950}$ catalyst may

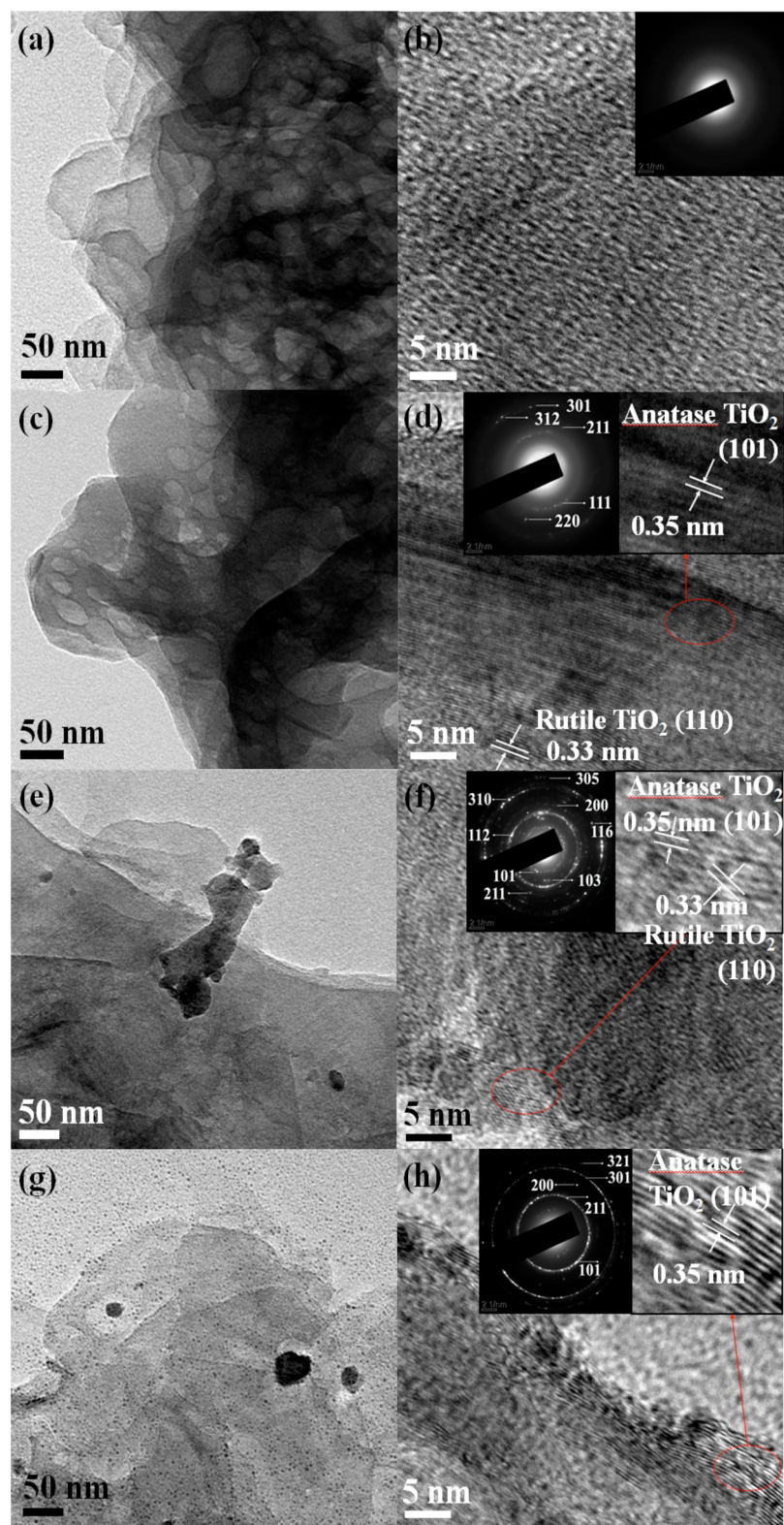


Fig. 4. TEM and HR-TEM images of (a, b) MCA@Ti₃C₂T_x, (c, d) TiO₂C@CN_{x,500}, (e, f) TiO₂C@CN_{x,700}, and (g, h) TiO₂C@CN_{x,950} composites (Inset: the selected area electron diffraction patterns).

be attributed to its highly stable chemical structure, along with the encapsulated TiO₂ nanoparticles physically isolated from the harsh environment, thus avoiding leaching. Additionally, current versus time (*I-t*) chronoamperometric measurement was performed to investigate the methanol tolerance of the TiO₂C@CN_{x,950} catalyst, which is a key parameter for practical applications (the inset of Fig. 5f). The current

for TiO₂C@CN_{x,950} is slightly changed, whereas a conspicuous decrease is observed in the current density for the commercial Pt/C catalyst, indicating that the TiO₂C@CN_{x,950} catalyst exhibits high selectivity for the ORR with a strong tolerance to crossover effects.

The enhanced ORR activity of the as-prepared TiO₂C@CN_{x,950} nanosheets could be attributed to the following reasons. (i) The carbonyl

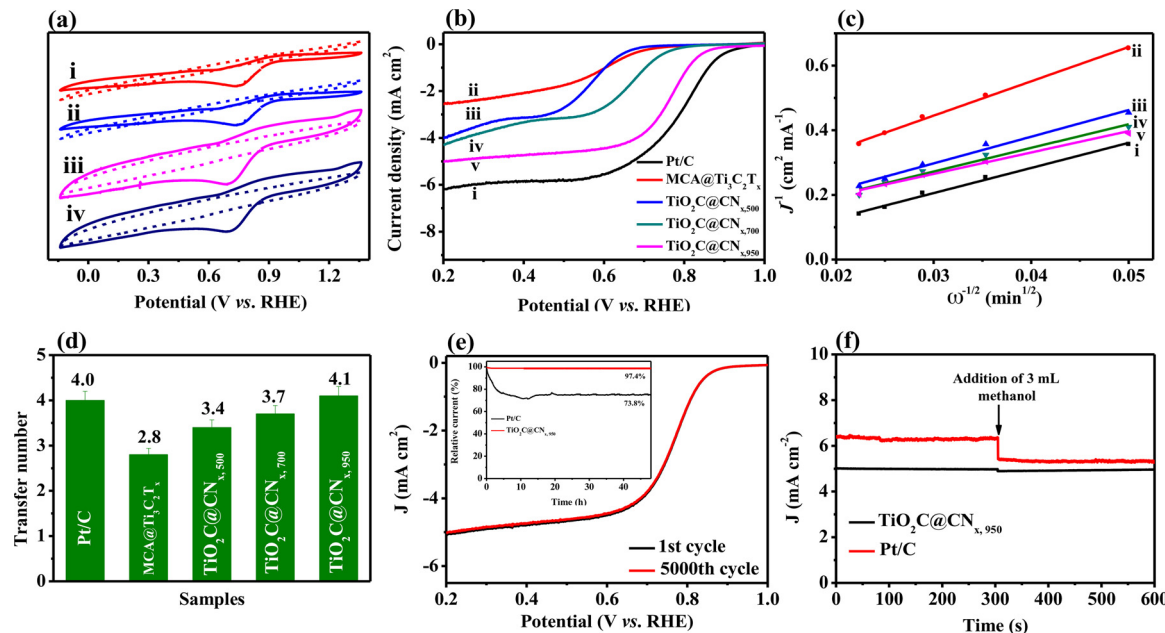


Fig. 5. (a) CVs recorded in an O_2 and N_2 -saturated 0.1 M KOH solution of (i) MCA@ $Ti_3C_2T_x$, (ii) $TiO_2C@CN_{x,500}$, (iii) $TiO_2C@CN_{x,700}$, and (iv) $TiO_2C@CN_{x,950}$, and (b) LSV curves of on RDE at 1600 rpm (i) Pt/C (20%), (ii) MCA@ $Ti_3C_2T_x$, (iii) $TiO_2C@CN_{x,500}$, (iv) $TiO_2C@CN_{x,700}$, and (v) $TiO_2C@CN_{x,950}$. (c) The corresponding linear K - L plots obtained from the LSV curves at different potentials of (i) Pt/C (20%), (ii) $TiO_2C@CN_{x,500}$, (iii) $TiO_2C@CN_{x,700}$, and (iv) $TiO_2C@CN_{x,950}$. (d) Electron transfer numbers of five kinds catalysts. (e) LSV curves before and after 5000 CV cycles in O_2 -saturated 0.1 M KOH solution of the $TiO_2C@CN_{x,950}$ ranging from 0.1 to 0.2 V vs. RHE (Inset: Current-time chronoamperometric response of Pt/C and $TiO_2C@CN_{x,950}$ in an O_2 -saturated KOH solution at a potential of 0.7 V). (f) Current-time (I - t) curves of $TiO_2C@CN_{x,950}$ and Pt/C in O_2 -saturated 0.1 M KOH solution without and with 3.0 mL MeOH solution at 0.7 V vs. RHE at 1600 rpm.

and carboxyl groups containing the graphene-like surface embedded with TiO_2 nanoparticles can provide good wettability in the electrolyte solution, further accelerating the diffusion and adsorption of O_2 molecules [42]; (ii) The carbon-coating layer with an improved electrocatalytic properties of TiO_2 enables the presence of oxygen vacancies and reduced Ti^{3+} and reduces the contact resistance between the active material particles [36]; and (iii) the porous structure of $TiO_2C@CN_{x,950}$ is not only beneficial for O_2 transmission and exposing several active sites but also is helpful to facilitate the transport of electrolyte ions, reaction intermediates, and products and prevents unwanted agglomeration of TiO_2 and Ti^{3+} active sites [43].

3.4. HER and OER electrocatalytic performances of all samples

The HER activities of the as-synthesized $TiO_2C@CN_x$ catalysts were investigated by LSV recorded in 0.5 M H_2SO_4 solution and compared with that of the benchmark Pt/C catalyst. The high cathodic current achieving the $TiO_2C@CN_{x,950}$ compared with other referenced samples suggests its promising HER catalytic activity. The efficacy of a HER catalyst is generally determined from the overpotential required to achieve an onset potential at 1 mA cm^{-2} (represented by η_0) and 10 mA cm^{-2} (represented by η_{10}). The η_0 and η_{10} values of all samples are summarized in Table S6. Among the series of $TiO_2C@CN_x$ composites (Fig. 6a), the $TiO_2C@CN_{x,950}$ catalyst exhibits good catalytic performance with a small η_0 value of -98.6 mV and η_{10} of -254.5 mV . These values are lower than those of MCA@ $Ti_3C_2T_x$ (η_0 of -256.5 mV and a η_{10} of -547.8 mV), $TiO_2C@CN_{x,500}$ (η_0 of -195.8 mV and a η_{10} of -415.1 mV), and $TiO_2C@CN_{x,700}$ (η_0 of -102.5 mV and a η_{10} of -279.0 mV) composites. This finding displays that η_{10} of $TiO_2C@CN_{x,950}$ catalyst (-254.5 mV) is slightly more negative than that of the state-of-the-art Pt/C catalyst (-88.1 mV). This result suggests the promising HER activity for the $TiO_2C@CN_{x,950}$ catalyst. Furthermore, the obtained η_{10} with $TiO_2C@CN_{x,950}$ is quite comparable to many previously reported HER electrocatalysts (Table S7). The Tafel slopes for $TiO_2C@CN_x$ catalysts and state-of-the-art Pt/C were evaluated from their corresponding Tafel plots (Fig. 6b). This condition

demonstrates that the Tafel slope of the $TiO_2C@CN_{x,950}$ catalyst is the smallest (60 mV dec^{-1}) among the series of $TiO_2C@CN_x$ catalysts and close to that of the commercial Pt/C catalyst (37 mV dec^{-1}). Turnover frequency (TOF) or turnover number (TON) is also a significant indicator used to evaluate HER electrocatalysts, which reveals the intrinsic electrocatalytic activity. The TOF values for Ti and N active sites of the series of $TiO_2C@CN_x$ nanosheets at 200 mV (vs. RHE) in 0.5 M H_2SO_4 were calculated based on the estimated numbers of active sites reported by Mahmood et al [44], separately. As shown in Fig. S15a, the TOF value of $TiO_2C@CN_{x,950}$ catalyst with respect to Ti active site is $0.314\text{ H}_2\text{ s}^{-1}$, which is larger than those of MCA@ $Ti_3C_2T_x$ ($0.146\text{ H}_2\text{ s}^{-1}$), $TiO_2C@CN_{x,500}$ ($0.144\text{ H}_2\text{ s}^{-1}$), and $TiO_2C@CN_{x,700}$ ($0.162\text{ H}_2\text{ s}^{-1}$) composites. Furthermore, the TOF value for N active site of $TiO_2C@CN_{x,950}$ ($0.096\text{ H}_2\text{ s}^{-1}$ at 200 mV) is also larger compared to other $TiO_2C@CN_x$ composites (Fig. S15b). The corresponding TONs of the samples were shown in Figs. S15c and S15d. It indicates the more active sites in $TiO_2C@CN_{x,950}$ catalyst, which further boost the electrochemical activities.

For comparison, the HER performances for the pristine MCA and CN_x nanosheets were also investigated, as displayed in Fig. S16. Meanwhile, the corresponding η_0 , η_{10} , and Tafel slopes are summarized in Table S8. The CN_x nanosheets give a very large η_0 of -295.3 mV , η_{10} of -548.0 mV , and a large Tafel slope of 214 mV dec^{-1} . The HER electrocatalysis becomes even poor for the pristine MCA, giving large η_0 , η_{10} , and Tafel slope values. This result signifies that a small amount of electrocatalytically active sites or low electrochemical activity is present in the CN_x nanosheets. Concurrently, the HER performances of the exfoliated $Ti_3C_2T_x$ and $TiO_2@C$ nanosheets were also measured (Fig. S17 and Table S9). The finding reveals that the obtained $TiO_2@C$ nanosheets exhibit high electrocatalytic activity, showing a small η_0 (-98.7 mV), η_{10} (-280.7 mV), and Tafel slope (74 mV dec^{-1}). These values are lower than those of the exfoliated $Ti_3C_2T_x$ nanosheets ($\eta_0 = -240.0\text{ mV}$, $\eta_{10} = -480.0\text{ mV}$, the Tafel slope = 145 mV dec^{-1}). Therefore, the presence of $TiO_2@C$ nanosheets can strengthen the HER performance of the obtained $TiO_2C@CN_{x,950}$ catalyst. Compared with other catalysts, $TiO_2C@CN_{x,950}$ shows superior HER

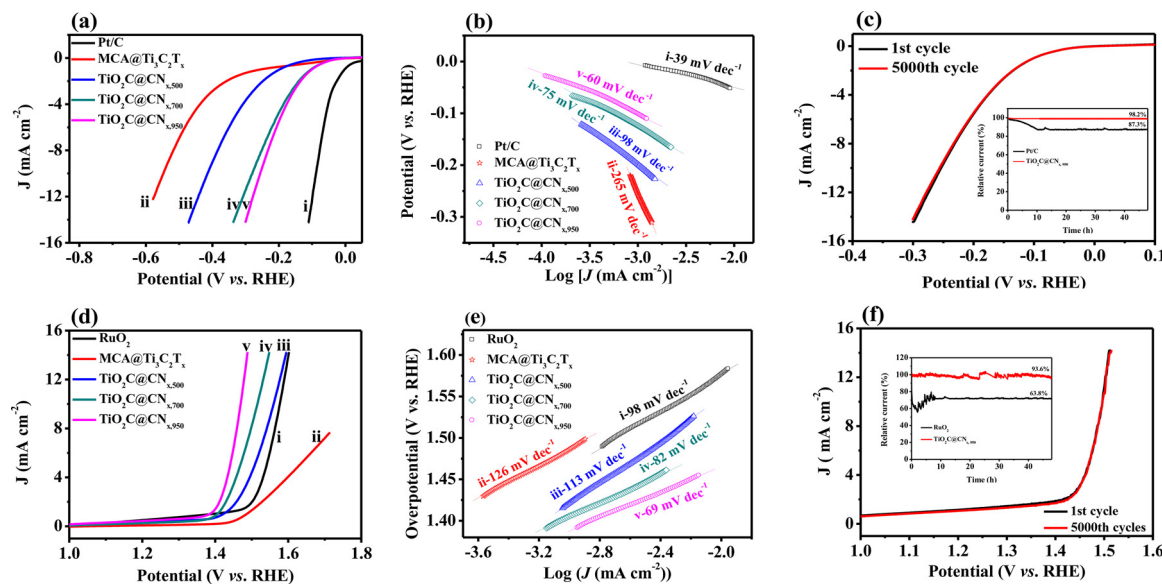


Fig. 6. HER performances of the series of $\text{TiO}_2\text{C}@\text{CN}_x$ composites. (a) Polarization curves and (b) the corresponding Tafel plots of (i) Pt/C (20%), (ii) $\text{MCA}@\text{Ti}_3\text{C}_2\text{T}_x$, (iii) $\text{TiO}_2\text{C}@\text{CN}_{x,500}$, (iv) $\text{TiO}_2\text{C}@\text{CN}_{x,700}$, and (v) $\text{TiO}_2\text{C}@\text{CN}_{x,950}$ composites. (c) Polarization curves of the $\text{TiO}_2\text{C}@\text{CN}_{x,950}$ in 0.5 M H_2SO_4 for the 1st and 5000th cycles between 0.1 and -0.4 V vs. RHE. The inset: time-dependent HER stability of the Pt/C and $\text{TiO}_2\text{C}@\text{CN}_{x,950}$ at a constant overpotential of -250 mV for 48 h in N_2 -saturated H_2SO_4 solution (0.5 M); OER performances of the various catalysts. (d) LSV curves of the different catalysts in 0.1 M KOH at a scan rate of 10 mV s^{-1} and (e) OER Tafel plots for the catalysts calculated from the LSV curves of (i) RuO_2 , (ii) $\text{MCA}@\text{Ti}_3\text{C}_2\text{T}_x$, (iii) $\text{TiO}_2\text{C}@\text{CN}_{x,500}$, (iv) $\text{TiO}_2\text{C}@\text{CN}_{x,700}$, and (v) $\text{TiO}_2\text{C}@\text{CN}_{x,950}$ composites; (f) The durability test of $\text{TiO}_2\text{C}@\text{CN}_{x,950}$ in N_2 -saturated 0.1 M KOH solution for the 1st and 5000th test between 1.0 and 1.6 V vs. RHE (Inset: time-dependent OER stability of the RuO_2 and $\text{TiO}_2\text{C}@\text{CN}_{x,950}$ at the applied current density of 10 mA cm^{-2} for 48 h in O_2 -saturated 0.1 M KOH solution).

performance to most of them (**Table S7**).

Additionally, the electrocatalytic HER performances of the series of $\text{TiO}_2\text{C}@\text{CN}_x$ catalysts in 1.0 M KOH solution were investigated, as illustrated in **Fig. S18**. The corresponding η_0 , η_{10} , and Tafel slopes are displayed in **Table S10**. As shown in **Fig. S18a**, the iR-corrected LSV curve for the $\text{TiO}_2\text{C}@\text{CN}_{x,950}$ nanosheets exhibits acceptable electrocatalytic activity, giving a cathodic current density of 10 mA cm^{-2} at -495.4 mV overpotential, which is considerably lower than those of $\text{TiO}_2\text{C}@\text{CN}_{x,500}$ (-782.8 mV) and $\text{TiO}_2\text{C}@\text{CN}_{x,700}$ (-623.3 mV). Furthermore, the Tafel slope is calculated as 133 mV dec^{-1} for the $\text{TiO}_2\text{C}@\text{CN}_{x,950}$ nanosheets (**Fig. S18b**). This finding indicates that the $\text{TiO}_2\text{C}@\text{CN}_{x,950}$ nanosheets can be applied as electrocatalysts for HER in both acidic and alkaline solutions, and therefore can be explored as the bifunctional catalyst for water splitting in alkaline solution.

Based on the above results, several reasons are proposed to explain the superior catalytic performance of $\text{TiO}_2\text{C}@\text{CN}_{x,950}$ for HER enumerated as follows. (i) The synergetic effects among the Ti core, nitrogen-doped graphene-like support, the oxygen vacancies with high content, and the additional active sites caused by the modulation of the electronic states of carbon by doping metal core with nitrogen plays an important role in enhancing the HER activity [45]; (ii) The CN_x nanostructure contained in $\text{TiO}_2\text{C}@\text{CN}_{x,950}$ is an oxygen-functionalized graphene-like sheet, and the carbonyl and carboxyl groups of CN_x are attached at the edges. These groups can stabilize the Ti^{3+} species, which would enhance the electrocatalytic ability [46]; and (iii) the porous $\text{TiO}_2\text{C}@\text{CN}_x$ nanostructure is beneficial for the transmission of ions and overflow of H_2 , leading to fast catalytic reactions [39].

We also evaluated OER performances of the $\text{TiO}_2\text{C}@\text{CN}_x$ composites and commercial RuO_2 catalyst in 0.1 M KOH solution (**Fig. 6d**). The corresponding η_0 , η_{10} , and Tafel slopes are summarized in **Table S11**. Among the series of $\text{TiO}_2\text{C}@\text{CN}_x$ composites, $\text{TiO}_2\text{C}@\text{CN}_{x,950}$ has a small η_0 of 1.39 V and η_{10} of 1.47 V, lower than those of $\text{MCA}@\text{Ti}_3\text{C}_2\text{T}_x$ (η_0 of 1.49 V), $\text{TiO}_2\text{C}@\text{CN}_{x,500}$ ($\eta_0 = 1.43$ V, $\eta_{10} = 1.56$ V), $\text{TiO}_2\text{C}@\text{CN}_{x,700}$ ($\eta_0 = 1.41$ V, $\eta_{10} = 1.52$ V), and RuO_2 ($\eta_0 = 1.48$ V, $\eta_{10} = 1.56$ V). This result means that the $\text{TiO}_2\text{C}@\text{CN}_{x,950}$ has the best OER performance among these samples. In addition, OER is further explored based on the Tafel slopes. As shown in **Fig. 6e**, the

$\text{TiO}_2\text{C}@\text{CN}_{x,950}$ catalyst exhibits a smaller Tafel slope of approximately 69 mV dec^{-1} compared with the exfoliated $\text{MCA}@\text{Ti}_3\text{C}_2\text{T}_x$ (126 mV dec^{-1}), $\text{TiO}_2\text{C}@\text{CN}_{x,500}$ (113 mV dec^{-1}), $\text{TiO}_2\text{C}@\text{CN}_{x,700}$ (82 mV dec^{-1}), and RuO_2 (98 mV dec^{-1}). The smallest Tafel slope value shows that the $\text{TiO}_2\text{C}@\text{CN}_{x,950}$ composite undergoes a favorable kinetics. Moreover, the OER performance of our $\text{TiO}_2\text{C}@\text{CN}_{x,950}$ outperforms other carbon nitrides and metal oxide catalysts (**Table S12**).

Additionally, the OER performances of pristine MCA and $\text{CN}_{x,950}$ were investigated (**Fig. S19** and **Table S13**). The result presents that the pristine MCA catalyst requires a very large η_0 of 1.55 V, along with a high Tafel slope of 132 mV dec^{-1} . Meanwhile, CN_x gives a small η_0 of 1.45 V and a Tafel slope of 180 mV dec^{-1} . All these findings reveal that the OER properties of both MCA and its derivative are poor. Furthermore, the $\text{Ti}_3\text{C}_2\text{T}_x$ nanosheets exhibit even inferior OER activity (**Fig. S20** and **Table S14**), giving a high Tafel slopes of 156 mV dec^{-1} , whereas the calcinated $\text{TiO}_2@\text{C}$ has a low value (108 mV dec^{-1}). Notably, the OER ability is improved after the combination of MCA and $\text{Ti}_3\text{C}_2\text{T}_x$ nanosheets, showing a lower Tafel slope of 126 mV dec^{-1} than that of each individual component. As aforementioned, the $\text{TiO}_2\text{C}@\text{CN}_{x,950}$ composite has high content of Ti^{3+} species. The predominant reduced Ti^{3+} can provide a high concentration of active sites for water adsorption and dissociation, which is a critical first step in OER. Additionally, the hierarchical pore structure facilitates the oxygen diffusion and allows sufficient electrolyte immersion onto the surfaces of the oxygen cathode, further improving the OER activity [47]. N-doping can introduce abundant atomic reactive sites and functional groups to effectively accelerate the OER processes to achieve good reversibility and excellent cyclability [48].

Durability and long-term stability, especially at high current densities, are essential qualities for an advanced HER and OER electrocatalyst. In this study, the $\text{TiO}_2\text{C}@\text{CN}_{x,950}$ exhibits impressive operational stability on catalytic performance (**Fig. 6c**). The accelerated degradation test reveals that the final polarization curves suffer minimal degradation compared with the initial ones after taking 5000 continuous cyclic voltammetric cycles. The chronoamperometry test demonstrates that the $\text{TiO}_2\text{C}@\text{CN}_{x,950}$ can keep working efficiently for more than 48 h (the inset of **Fig. 6c**) at high current densities, whereas

the Pt/C catalyst shows a high current density loss of 12.7%. Additionally, the stability test of $\text{TiO}_2\text{C@CN}_{x,950}$ toward OER was performed for 5000 CV cycles (Fig. 6f). The LSV curve for the $\text{TiO}_2\text{C@CN}_{x,950}$ electrode has no obvious degradation even after 5000 potential cycles. The time-dependent current density ($I-t$) curve (the inset of Fig. 6f) shows only 6.4% variation after 48 h, whereas the commercial RuO_2 catalyst exhibits a high current loss (36.2%). Consequently, we believe that the high stability of our $\text{TiO}_2\text{C@CN}_{x,950}$ catalyst is due to the highly stable chemical performances of the rutile TiO_2 and abundant active sites.

Moreover, the tolerance toward methanol for the $\text{TiO}_2\text{C@CN}_{x,950}$ and Pt/C materials was evaluated using chronoamperometry measurements in 0.5 M H_2SO_4 and 0.1 M KOH with the addition of 3.0 M methanol for HER and OER, respectively. As shown in Fig. S21a, the HER current density of the commercial Pt/C catalyst exhibits an intense decrease when 3.0 M methanol is injected, whereas the current of $\text{TiO}_2\text{C@CN}_{x,950}$ catalyst only displays a slight methanol crossover effect. Therefore, this result indicates that the as-synthesized $\text{TiO}_2\text{C@CN}_{x,950}$ electrocatalyst provides an excellent electrocatalytic activity, persistent stability, and the superb ability of resistance to methanol. Furthermore, the samples were measured by chronoamperometric measurements for OER at 0.7 V (vs. RHE) in O_2 -saturated 0.1 M KOH electrolyte at a rotating speed of 1600 rpm for 600 s while 3.0 M methanol was added at 300 s. As shown in Fig. S21b, after methanol introduction, the voltammetric current of RuO_2 electrode increases instantaneously. However, the $\text{TiO}_2\text{C@CN}_{x,950}$ slightly changes during the same process. In summary, all of these results verify that the $\text{TiO}_2\text{C@CN}_{x,950}$ catalyst can not only maintain excellent stability in alkaline solution but also exhibit insensitivity to methanol.

It can be seen from the above electrocatalytic performances, the CN_x derived from MCA possessed excellent ORR activity, whereas $\text{TiO}_2@\text{C}$ produced by $\text{Ti}_3\text{C}_2\text{T}_x$ only showed poor ORR performance (Tables S2–S4). As for the HER (Tables S6, S8 and S9) and OER (Tables S11, S13 and S14), the opposite trends were observed. The $\text{TiO}_2@\text{C}$ exhibits much higher electrocatalytic activities than that of CN_x . Therefore, the excellent electrocatalytic activity of $\text{TiO}_2@\text{CN}_x$ for HER/OER/ORR are ascribed to the synergistic effect between $\text{TiO}_2@\text{C}$ and CN_x . It means that the presence of CN_x can boost ORR activity of the obtained $\text{TiO}_2\text{C@CN}_x$ catalyst, while the $\text{TiO}_2@\text{C}$ nanosheets can strengthen the HER and OER performances of composite. Additionally, Tables S2, S6, and S11 display that the ORR/HER/OER performances of the $\text{TiO}_2\text{C@CN}_{x,950}$ composite outperforms $\text{TiO}_2\text{C@CN}_{x,500}$ and $\text{TiO}_2\text{C@CN}_{x,700}$. It suggests that the calcination temperature has an effect on the chemical structure of the composite and dispersion of the TiO_2 particles. Hence, $\text{TiO}_2@\text{C}$ and CN_x can boost the synergistic effect only when MCA@ $\text{Ti}_3\text{C}_2\text{T}_x$ was calcinated at a suitable temperature.

Furthermore, in order to further understand whether the use of Pt wire as a counter electrode has an effect on the test results under acidic conditions or not, the polarization curve of $\text{TiO}_2\text{C@CN}_{x,950}$ nanosheets toward HER by using the graphite rod as counter electrode was measured in 0.5 M H_2SO_4 solution in order to compare with the result of Pt wire. As shown in Fig. S22a, two obtained polarization curves are completely coincident, indicating that the Pt wire as counter electrode was not be dissolved in acidic media during the electrochemical measurements for HER. The polarization curves of $\text{TiO}_2\text{C@CN}_{x,950}$ nanosheets toward OER in 0.1 M KOH using Pt wire and graphite rod as counter electrode, respectively, were also compared (Fig. S22b). There is also no difference between these two curves. Consequently, it can be concluded that the use of Pt wire as counter electrode can not affect catalytic properties of the materials during electrochemical measurements.

To verify the excellent electrochemical properties toward ORR, HER, and OER of the $\text{TiO}_2\text{C@CN}_{x,950}$ catalyst, estimating the ECSA is necessary because high active surface area can lead to high number of active sites and normally excellent catalytic activity. CV was carried out in a potential window of 0.1–0.2 V (vs. Hg/HgO reference electrode) at

various scan rates of 5, 10, 15, 20, 25, 30, and 50 mV s^{-1} (Figs. S23a–d). Afterward, a linear slope obtained by plotting capacitive current ($j_{\text{anodic}} - j_{\text{cathodic}}$) at 0.2 V against scan rates is equivalent to twice of the double layer capacitance (C_{dl}) value, which can represent the ECSA [49]. As displayed in Fig. S23e, the electrochemical results reveal that the $\text{TiO}_2\text{C@CN}_{x,950}$ catalyst has a C_{dl} of 16.0 m F cm^{-2} . This value is higher than that of other two samples, i.e., MCA@ $\text{Ti}_3\text{C}_2\text{T}_x$ (1.2 m F cm^{-2}), $\text{TiO}_2\text{C@CN}_{x,500}$ (6.4 m F cm^{-2}), and $\text{TiO}_2\text{C@CN}_{x,700}$ (11.5 m F cm^{-2}). This condition indicates that the $\text{TiO}_2\text{C@CN}_{x,950}$ catalyst exhibits a large electroactive surface area, partially boosting the electrocatalytic reactions. To further investigate the kinetics of the as-developed catalyst, electrochemical impedance spectroscopy measurements were concurrently performed at a potential of -0.24 and -0.45 V in the frequency range from 0.01 Hz to 100 kHz in 0.5 M H_2SO_4 and 0.1 M KOH solution, respectively. Fig. S24a shows the Nyquist plots of the $\text{TiO}_2\text{C@CN}_x$ -modified GCE in 0.5 M H_2SO_4 . The semicircle diameter reflects the charge-transfer resistance (R_{ct}) of the electrode–electrolyte interface. The R_{ct} value of the $\text{TiO}_2\text{C@CN}_{x,950}$ is estimated to be the smallest value (53.6Ω) among the series of $\text{TiO}_2\text{C@CN}_x$, comparable with those of many other reported carbon nitride catalysts [50–52]. Simultaneously, the smallest R_{ct} value of $\text{TiO}_2\text{C@CN}_{x,950}$ -modified GCE (197.2Ω) in 0.1 M KOH solution is also obtained (Fig. S24b). In consequence, the $\text{TiO}_2\text{C@CN}_{x,950}$ offers fast charge transfer at the electrode–electrolyte interface and provides high electrocatalytic activity. The high charge-transfer capacity of the $\text{TiO}_2\text{C@CN}_{x,950}$ electrode is mainly due to the superb electrical contact originated from the extended conjugated $\pi-\pi^*$ electronic structure and the high surface area [53], the ultrathin nanosheets, which enables all of the active sites on the surface to expose, and electrons that can transport in $\text{TiO}_2@\text{C}$ layers and penetrate into the CN_x layers through the contact area [54].

Since the ratio of two components in the composite materials affects the properties of the final product, we also investigated the effect of precursor ratio ($\text{Ti}_3\text{C}_2\text{T}_x$ and MCA) on the catalytic properties of the $\text{TiO}_2\text{C@CN}_x$ composites. Apart from the dosage (50 mg) of $\text{Ti}_3\text{C}_2\text{T}_x$ as aforementioned, the dosages of $\text{Ti}_3\text{C}_2\text{T}_x$ added in composite were used as 30 and 70 mg, separately. Consequently, the mass ratios of the $\text{Ti}_3\text{C}_2\text{T}_x$ and MCA in three sample are 3:100, 5:100 and 7:100, respectively. As shown in the Fig. S25, when the ratio of $\text{Ti}_3\text{C}_2\text{T}_x$ to MCA was 3:100, the electrocatalytic activities of the corresponding composite toward HER, OER and ORR were significantly declined. When the ratio of $\text{Ti}_3\text{C}_2\text{T}_x$ to MCA was 7:100, the electrocatalytic performance was also reduced. It suggests that large amounts of $\text{Ti}_3\text{C}_2\text{T}_x$ can result in the agglomeration of TiO_2 and Ti^{3+} active sites, further lessening the catalytic reactions. Moreover, the less dosage of $\text{Ti}_3\text{C}_2\text{T}_x$ also weakens the synergistic effect among different components. Thereby, in the present work, the mass ratio of 5:100 of $\text{Ti}_3\text{C}_2\text{T}_x$ to MCA was used for all electrochemical measurements.

3.5. Water-splitting performance for the $\text{TiO}_2\text{C@CN}_{x,950}$ catalyst in the alkaline solution

Inspired by the superior OER and HER performances of $\text{TiO}_2\text{C@CN}_{x,950}$, overall water splitting was conducted in a 0.1 M KOH solution with $\text{TiO}_2\text{C@CN}_{x,950}$ loaded on two pieces of Ni foam (NF) serving as cathode and anode (Fig. 7a). When the cell voltage between the anode and cathode is increased to over 1.42 V, the catalytic current starts to increase substantially. Concurrently, a large number of bubbles are produced on the surface of both $\text{TiO}_2\text{C@CN}_{x,950}$ -modified NF electrodes and 1.45 and 1.5 V of the onset potential for $\text{TiO}_2\text{C@CN}_{x,700}$ and $\text{TiO}_2\text{C@CN}_{x,500}$, respectively. This result indicates that the $\text{TiO}_2\text{C@CN}_{x,950}$ catalyst indeed effectively catalyze both HER and OER concurrently. Particularly, the current density of 10 mA cm^{-2} is reached at a cell voltage of 1.50 V in 0.1 M KOH solution, corresponding to a combined overpotential (at both anode and cathode) of only 143 mV for overall water splitting. This condition is much better

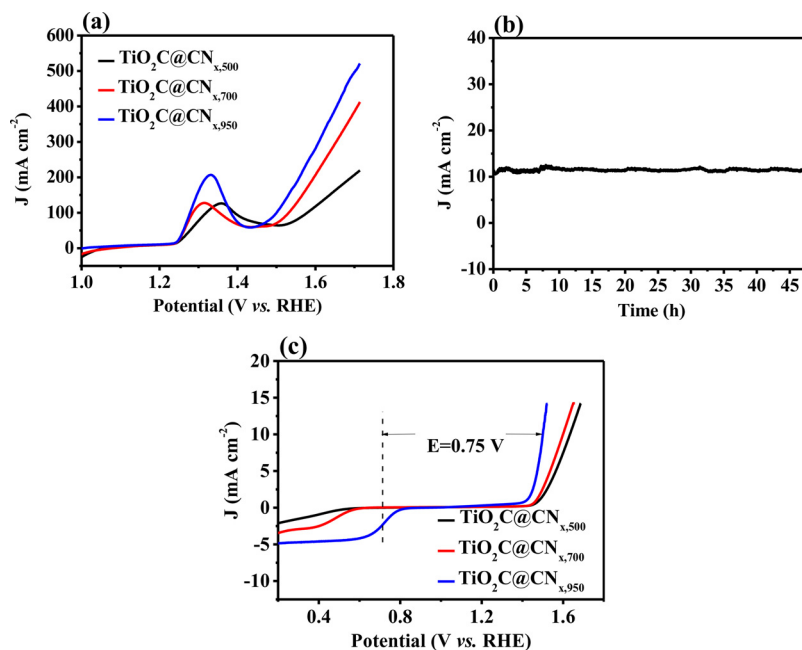


Fig. 7. (a) Polarization curves of (i) TiO₂C@CN_{x,500}, (ii) TiO₂C@CN_{x,700}, (iii) TiO₂C@CN_{x,950} in the two-electrode electrolyzers at the scan rate of 5 mV s⁻¹. (b) Long-term durability test of the TiO₂C@CN_{x,950} electrolyzer at 10 mA cm⁻². (c) The overall LSV curves in the potential range of 0.32–1.62 V of (i) TiO₂C@CN_{x,500}, (ii) TiO₂C@CN_{x,700}, (iii) TiO₂C@CN_{x,950}, ΔE ($E_j = \eta_{10} - E_{1/2}$) isometric for bifunctional ORR and OER activities, the rotating speed is 1600 rpm. Inset: the values of ΔE for the series of TiO₂C@CN_x catalysts (see text).

than other reported electrodes (Table S15), such as NiFe LDH/Ni foam (1.70 V@10 mA cm⁻²), EG/Co_{0.85}Se/NiFeLDH (1.67 V@10 mA cm⁻²), and Co-N_x|P-GC/FEG (1.60 V@10 mA cm⁻²). Additionally, the TiO₂C@CN_{x,950}||TiO₂C@CN_{x,950}/NF electrolyzer exhibits exceptionally long-term stability with a negligible overpotential loss within 48 h (Fig. 7b). Thereby, the TiO₂C@CN_{x,950} nanosheets serve as a very promising candidate catalyst for practical alkaline water electrolysis applications.

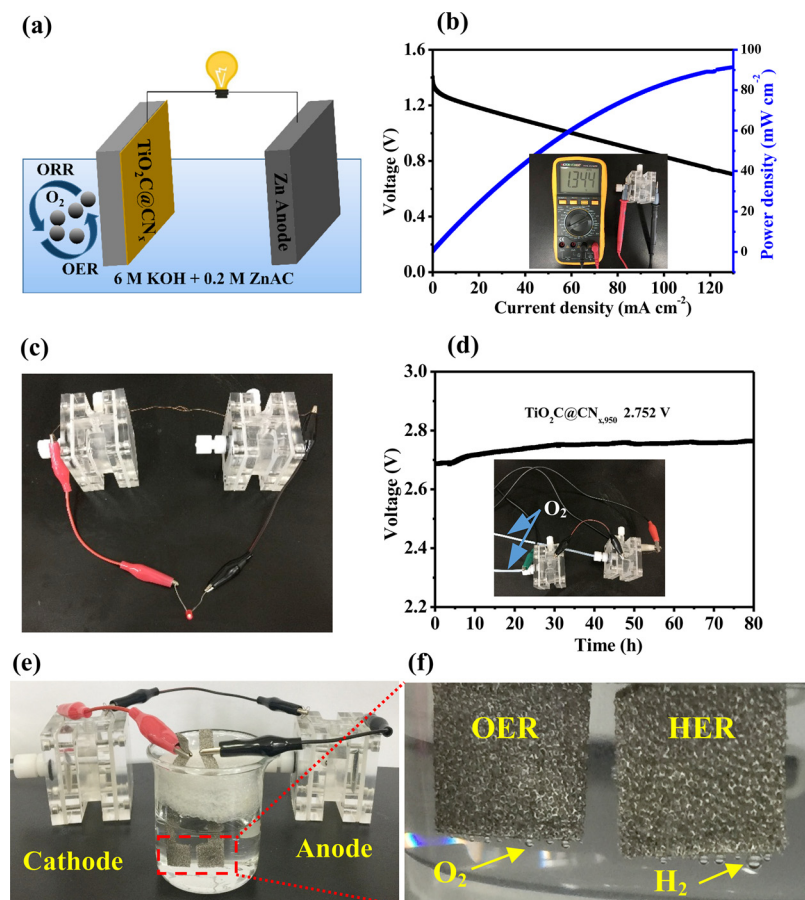
The above results show that the TiO₂C@CN_x might be an attractive candidate electrocatalyst for both OER and ORR in alkaline solution. The overall oxygen activity of the series of TiO₂C@CN_x nanosheets as a bifunctional catalyst can be determined by the potential difference (ΔE) between the $E_j = 10$ for OER and $E_{1/2}$ for ORR. The small ΔE indicates the good reversible oxygen electrode. As shown in Fig. 7c, the TiO₂C@CN_{x,950} exhibits a ΔE of 0.75 V. This value is much lower than those of other two electrocatalysts, including TiO₂C@CN_{x,500} ($\Delta E = 1.08$ V) and TiO₂C@CN_{x,700} ($\Delta E = 0.94$ V) and is much better than other reported electrodes (Table S16). As a result, the TiO₂C@CN_{x,950} catalyst is a promising low cost, efficient trifunctional catalyst for HER, ORR, and OER simultaneously. The excellent trifunctional electrocatalytic performances for HER, OER, and ORR of the as-prepared TiO₂C@CN_{x,950} are ascribed to three main reasons, namely, the synergistic effect among the Ti core, nitrogen-doped graphene-like support, and the oxygen vacancies, the high stability of the formed Ti³⁺ species by the grapheme-like chemical and nanostructure, and the porous layers of the TiO₂C@CN_{x,950}. All of these contributions can not only increase the active sites and enhance the electrochemical activity but also promote the water molecule adsorption and accelerate the flow of the produced H₂ and O₂. Finally, inspection of the post-HER and OER reaction of TiO₂C@CN_{x,950} shows that the catalysts' morphologies are well preserved (Fig. S26a) with nearly unchanged crystallographic structure (Figs. S26b–e). This finding indicates that the TiO₂C@CN_{x,950} catalyst is very stable and can keep high electrocatalytic activity for long duration reaction.

Based on the trifunctionally catalytic activity for TiO₂C@CN_{x,950} nanosheets, a Zn-air battery was constructed using a zinc plate as the anode, TiO₂C@CN_{x,950} as the air cathode, and 6.0 M KOH and 0.2 M zinc acetate as the electrolyte (Fig. 8a). Fig. 8b presents the polarization and power density curves for the Zn-air battery equipped with the TiO₂C@CN_{x,950} catalyst, giving the maximum power density of 91.8 mW cm⁻². The open-circuit potential shows 1.344 V, that is close

to that of Pt/C air cathode of 1.47 V (the inset in Fig. 8b) [55]. Furthermore, a red light-emitting diode (LED, ≈ 3.0 V) can be powered by two Zn-air cells in series with the TiO₂C@CN_{x,950} nanosheets as the air cathode (Fig. 8c), suggesting its promising applications in Zn-air batteries. Also, Fig. 8d shows that the Zn-air battery-driven water-splitting device exhibits good stability at 2.752 V as long as 80 h in 1.0 M KOH solution. Therefore, it can be concluded that electrons can move directly from the anode to cathode, further providing an electrical power and producing H₂ at the cathode and O₂ at the anode [56], as shown in Fig. 8e. It displays the two-electrode water-splitting device can be powered by two Zn-air batteries in series using TiO₂C@CN_{x,950} as the electrocatalyst in 1.0 M KOH. The clear gas bubbles produced both on the anode and cathode in enlarged image of Fig. 8e reveal a great potential of the TiO₂C@CN_{x,950} nanosheets for practical applications in overall water splitting (Fig. 8f).

4. Conclusion

We reported a new class of composite electrocatalysts by compounding MXene Ti₃C₂T_x and MCA, further calcinated into the TiO₂C@CN_x nanosheets at different temperatures. With the increasing temperature from 500 to 950 °C, the as-obtained TiO₂C@CN_x nanosheets exhibit several graphene-like nanostructure encapsulated with the TiO₂ nanoparticles. Remarkably, the TiO₂C@CN_{x,950} catalyst demonstrates multiple function to catalyze the OER, HER, or ORR in alkaline media due to the synergistic effect among different components. The TiO₂C@CN_{x,950} shows advantages of low cost, high efficiency, and good stability in electrocatalysis. Electrochemical measurements confirm that formation of TiO₂ and graphene-like nanosheets containing the TiO₂C@CN_{x,950} composite have an important role in the improved electrocatalytic performance. As a novel electrocatalyst for water splitting, the TiO₂C@CN_{x,950} catalyst gives a water-splitting current density of 10 mA cm⁻² was achieved at a low cell voltage of 1.50 V vs. RHE. Meanwhile, the overall oxygen activity of the TiO₂C@CN_{x,950} also outperforms other reported carbon nitrides and metal oxides, giving a small potential difference between the $E_{j=10}$ for OER and $E_{1/2}$ for ORR (0.75 V). Finally, we constructed a simply equipped liquid Zn-air battery using the proposed TiO₂C@CN_{x,950} catalyst, which produced a high open-circuit potential of 1.344 V and could supply an electrical power and producing H₂ at the cathode and O₂ at the anode. The work may open a new avenue to prepare a promising Pt-alternative catalyst for



developing multifunctional electrocatalysts for water splitting and liquid Zn-air battery.

Acknowledgements

This work was supported by the National Natural Science Foundation of China (Nos. 21601161 and U1604127), Program for Science & Technology Innovation Talents in Universities of Henan Province (No. 19HASTIT050), the Key Research Project of University of Henan Province (No. 19zx004), Backbone Teacher Project (No. 2017GGJS091) and Innovative Technology Team of Henan Province (No. CXTD2014042).

Appendix A. Supplementary data

Supplementary material related to this article can be found, in the online version, at doi:<https://doi.org/10.1016/j.apcatb.2019.02.033>.

References

- [1] S. Dutta, A. Indra, Y. Feng, H. Han, T. Song, Promoting electrocatalytic overall water splitting with nanohybrid of transition metal nitride-oxynitride, *Appl. Catal. B* 241 (2019) 521–527.
- [2] P. Liu, D. Gao, W. Xiao, L. Ma, K. Sun, P. Xi, D. Xue, J. Wang, Self-powered water-splitting devices by core-shell NiFe@N-graphite-based Zn-air batteries, *Adv. Funct. Mater.* 28 (2018) 1706928.
- [3] Y. Cheng, F. Liao, W. Shen, L. Liu, B. Jiang, Y. Li, M. Shao, Carbon cloth supported cobalt phosphide as multifunctional catalysts for efficient overall water splitting and zinc-air batteries, *Nanoscale* 9 (2017) 18977–18982.
- [4] M. Sakthivel, J.F. Drillet, An extensive study about influence of the carbon support morphology on Pt activity and stability for oxygen reduction reaction, *Appl. Catal. B* 231 (2018) 62–72.
- [5] B. Cui, B. Hu, J. Liu, M. Wang, Y. Song, K. Tian, Z. Zhang, L. He, Solution-plasma-assisted bimetallic oxide alloy nanoparticles of Pt and Pd embedded within two-dimensional Ti₃C₂T_x nanosheets as highly active electrocatalysts for overall water splitting, *ACS Appl. Mater. Interface* 10 (2018) 23858–23873.
- [6] Y. Zhang, M. Li, B. Hua, Y. Wang, Y. Sun, J. Luo, A strongly cooperative spinel nano-hybrid as an efficient bifunctional oxygen electrocatalyst for oxygen reduction reaction and oxygen evolution reaction, *Appl. Catal. B* 236 (2018) 413–419.
- [7] M.P. Karthikayini, G. Wang, P.A. Bhobe, A. Sheelam, V.K. Ramani, K.R. Priolkar, R.K. Raman, Effect of protonated amine molecules on the oxygen reduction reaction on metal-nitrogen-carbon-based catalysts, *Electrocatalysis-US* 8 (2016) 1–12.
- [8] J. Guo, Y. Li, Y. Cheng, L. Dai, Z. Xiang, Highly efficient oxygen reduction reaction electrocatalysts synthesized under nanospace confinement of metal-organic framework, *ACS Nano* 11 (2017) 8379–8386.
- [9] Z. Zhang, M. Dou, H. Liu, L. Dai, F. Wang, A facile route to bimetal and nitrogen-doped 3D porous graphitic carbon networks for efficient oxygen reduction, *Small* 12 (2016) 4193–4199.
- [10] M. Okubo, A. Sugahara, S. Kajiyama, A. Yamada, MXene as a charge storage host, *Acc. Chem. Res.* 51 (2018) 591–599.
- [11] T. Cai, L. Wang, Y. Liu, S. Zhang, W. Dong, H. Chen, X. Yi, J. Yuan, X. Xia, C. Liu, S. Luo, Ag₃PO₄/Ti₃C₂ MXene interface materials as a Schottky catalyst with enhanced photocatalytic activities and anti-photocorrosion performance, *Appl. Catal. B* 239 (2018) 545–554.
- [12] Z.W. Seh, K.D. Fredrickson, B. Anasori, J. Kibsgaard, A.L. Strickler, M.R. Lukatskaya, Y. Gogotsi, T.F. Jaramillo, A. Vojvodic, Two-dimensional molybdenum carbide (MXene) as an efficient electrocatalyst for hydrogen evolution, *ACS Energy Lett.* 1 (2016) 589–594.
- [13] J. Liu, Y. Liu, D. Xu, Y. Zhu, W. Peng, Y. Li, F. Zhang, X. Fan, Hierarchical “nanoroll” like MoS₂/Ti₃C₂T_x hybrid with high electrocatalytic hydrogen evolution activity, *Appl. Catal. B* 241 (2019) 89–94.
- [14] Z. Zhang, H. Li, G. Zou, C. Fernandez, B. Liu, Q. Zhang, J. Hu, Q. Peng, Self-reduction synthesis of new MXene/Ag composites with unexpected electrocatalytic activity, *ACS Sustain. Chem. Eng.* 4 (2016) 6763–6771.
- [15] M. Naguib, O. Mashtalar, M.R. Lukatskaya, B. Dyatkin, C. Zhang, V. Presser, Y. Gogotsi, M.W. Barsoum, One-step synthesis of nanocrystalline transition metal oxides on thin sheets of disordered graphitic carbon by oxidation of MXenes, *Chem. Commun.* 50 (2014) 7420–7423.
- [16] H. Ghassemi, W. Harlow, O. Mashtalar, M. Beidaghi, M.R. Lukatskaya, Y. Gogotsi, M.L. Taheri, In situ environmental transmission electron microscopy study of oxidation of two-dimensional Ti₃C₂ and formation of carbon-supported TiO₂, *J. Mater. Chem. A* 2 (2014) 14339–14343.
- [17] D.N. Pei, G. Li, A.Y. Zhang, Z. Xing, J.J. Chen, M. Yang, H.Q. Yu, Defective titanium dioxide single crystals exposed by high-energy {001} facets for efficient oxygen reduction, *Nat. Commun.* 6 (2015) 8696.
- [18] R.B. Rakhi, B. Ahmed, M.N. Hedhili, D.H. Anjum, H.N. Alshareef, Effect of post-treatment

- annealing gas composition on the structural and electrochemical properties of Ti_2CT_x MXene electrodes for supercapacitor applications, *Chem. Mater.* 27 (2015) 5314–5323.
- [19] W. Yuan, L. Cheng, Y. An, S. Lv, H. Wu, X. Fan, Y. Zhang, X. Guo, J. Tang, Laminated hybrid junction of sulfur-doped TiO_2 and a carbon substrate derived from Ti_3C_2 MXenes: Toward highly visible light-driven photocatalytic hydrogen evolution, *Adv. Sci.* 5 (2018) 1700870.
- [20] M. Yu, S. Zhou, Z. Wang, J. Zhao, J. Qiu, Boosting electrocatalytic oxygen evolution by synergistically coupling layered double hydroxide with MXene, *Nano Energy* 44 (2018) 181–190.
- [21] T. Varga, G. Ballai, L. Vásárhelyi, H. Haspel, Á. Kukovecz, Z. Kónya, Co₄N/nitrogen-doped graphene: a non-noble metal oxygen reduction electrocatalyst for alkaline fuel cells, *Appl. Catal. B* 237 (2018) 826–834.
- [22] L. He, B. Cui, J. Liu, M. Wang, Z. Zhang, H. Zhang, Fabrication of porous Co₃O₄/mC@MoS₂ composite loaded on g-C₃N₄ nanosheets as a highly efficient dual electrocatalyst for oxygen reduction and hydrogen evolution reactions, *ACS Sustain. Chem. Eng.* 6 (2018) 9257–9268.
- [23] S. Wang, P. He, L. Jia, M. He, T. Zhang, F. Dong, M. Liu, H. Liu, Y. Zhang, C. Li, J. Gao, L. Bian, Nanocoral-like composite of nickel selenide nanoparticles anchored on two-dimensional multi-layered graphitic carbon nitride: a highly efficient electrocatalyst for oxygen evolution reaction, *Appl. Catal. B* 243 (2019) 463–469.
- [24] C. Zhou, C. Lai, D. Huang, G. Zeng, C. Zhang, M. Cheng, L. Hu, J. Wan, W. Xiong, M. Wen, X. Wen, L. Qin, Highly porous carbon nitride by supramolecular pre-assembly of monomers for photocatalytic removal of sulfamethazine under visible light driven, *Appl. Catal. B* 220 (2018) 202–210.
- [25] L. Zhao, X. Sui, J. Li, J. Zhang, L. Zhang, G. Huang, Z. Wang, Supramolecular assembly promoted synthesis of three-dimensional nitrogen doped graphene frameworks as efficient electrocatalyst for oxygen reduction reaction and methanol electrooxidation, *Appl. Catal. B* 231 (2018) 224–233.
- [26] Y. Guo, J. Li, Y. Yuan, L. Li, M. Zhang, C. Zhou, Z. Lin, A rapid microwave-assisted thermolysis route to highly crystalline carbon nitrides for efficient hydrogen generation, *Angew. Chem. Int. Ed.* 55 (2016) 14693–14697.
- [27] J. Sun, J. Xu, A. Grafmueller, X. Huang, C. Liedel, G. Algara-Siller, M. Willinger, C. Yang, Y. Fu, X. Wang, M. Shalom, Self-assembled carbon nitride for photocatalytic hydrogen evolution and degradation of p-nitrophenol, *Appl. Catal. B* 205 (2017) 1–10.
- [28] Y. Yuan, L. Yin, S. Cao, L. Gu, G. Xu, P. Du, H. Chai, Y. Liao, C. Xue, Microwave-assisted heating synthesis: A general and rapid strategy for large-scale production of highly crystalline g-C₃N₄ with enhanced photocatalytic H₂ production, *Green Chem.* 16 (2014) 4663–4668.
- [29] L. He, Y. Liu, M. Lin, J. Awika, D.R. Ledoux, H. Li, A. Mustapha, A new approach to measure melamine, cyanuric acid, and melamine cyanurate using surface enhanced Raman spectroscopy coupled with gold nanosubstrates, *Sens. Instr. Food Qual.* 2 (2008) 66–71.
- [30] B. Zhao, P. Liu, Y. Jiang, D. Pan, H. Tao, J. Song, T. Fang, W. Xu, Supercapacitor performances of thermally reduced graphene oxide, *J. Power Sources* 198 (2012) 423–427.
- [31] C. Gu, N. Huang, Y. Chen, H. Zhang, S. Zhang, F. Li, Y. Ma, D. Jiang, Porous organic polymer films with tunable work functions and selective hole and electron flows for energy conversions, *Angew. Chem. Int. Ed.* 55 (2016) 3049–3053.
- [32] L. Bai, Q. Gao, Y. Zhao, Two fully conjugated covalent organic frameworks as anode materials for lithium ion batteries, *J. Mater. Chem. A* 4 (2016) 14106–14110.
- [33] G. Zhu, S. Shi, M. Liu, L. Zhao, M. Wang, X. Zheng, J. Gao, J. Xu, Formation of strong basicity on covalent triazine frameworks as catalysts for the oxidation of methylene compounds, *ACS Appl. Mater. Interface* 10 (2018) 12612–12617.
- [34] S.R. Carpenter, N.F. Caraco, D.L. Correll, R.W. Howarth, A.N. Sharpley, V.H. Smith, Nonpoint pollution of surface waters with phosphorus and nitrogen, *Ecol. Appl.* 8 (1998) 559–568.
- [35] J. Li, S. Wang, Y. Du, W. Liao, Enhanced photocatalytic performance of TiO₂@C nanosheets derived from two-dimensional Ti₂CT_x, *Ceram. Int.* 44 (2018) 7042–7046.
- [36] R. Boppella, J. Lee, F.M. Mota, J.Y. Kim, Z. Feng, D.H. Kim, Composite hollow nanostructures composed of carbon-coated Ti³⁺ self-doped TiO₂-reduced graphene oxide as an efficient electrocatalyst for oxygen reduction, *J. Mater. Chem. A* 5 (2017) 7072–7080.
- [37] F. Liu, K. Huang, Q. Wu, S. Dai, Solvent-free self-assembly to the synthesis of nitrogen-doped ordered mesoporous polymers for highly selective capture and conversion of CO₂, *Adv. Mater.* 29 (2017) 1700445.
- [38] J. Yu, W. Zhou, T. Xiong, A. Wang, S. Chen, B. Chu, Enhanced electrocatalytic activity of Co@N-doped carbon nanotubes by ultrasmall defect-rich TiO₂ nanoparticles for hydrogen evolution reaction, *Nano Res.* 10 (2017) 2599–2609.
- [39] S. Deng, Y. Zhong, Y. Zeng, Y. Wang, X. Wang, X. Lu, X. Xia, J. Tu, Hollow TiO₂@Co₉S₈ core-branch arrays as bifunctional electrocatalysts for efficient oxygen/ydrogen production, *Adv. Sci.* 5 (2018) 1700772.
- [40] D. Guo, R. Shibuya, C. Akiba, S. Saji, T. Kondo, J. Nakamura, Active sites of nitrogen-doped carbon materials for oxygen reduction reaction clarified using model catalysts, *Science* 351 (2016) 361–365.
- [41] Y. Dong, Y. Deng, J. Zeng, H. Song, S. Liao, A high-performance composite ORR catalyst based on the synergy between binary transition metal nitride and nitrogen-doped reduced graphene oxide, *J. Mater. Chem. A* 5 (2017) 5829–5837.
- [42] J. Yu, Z. Liu, L. Zhai, T. Huang, J. Han, Reduced graphene oxide supported TiO₂ as high performance catalysts for oxygen reduction reaction, *Int. J. Hydrogen Energy* 41 (2016) 3436–3445.
- [43] H. Wang, S. Ishihara, K. Ariga, Y. Yamauchi, All-metal layer-by-layer films: Bimetallic alternate layers with accessible mesopores for enhanced electrocatalysis, *J. Am. Chem. Soc.* 134 (2012) 10819–10821.
- [44] J. Mahmood, F. Li, S. Jung, M.S. Okyay, I. Ahmad, S. Kim, N. Park, H.Y. Jeong, J. Baek, An efficient and pH-universal ruthenium-based catalyst for the hydrogen evolution reaction, *Nat. Nanotechnol.* 12 (2017) 441.
- [45] W. Zhou, Z. Yin, X. Du Yaping, Z. Huang, Z. Zeng, H. Fan, J. Liu, H. Wang, Zhang, Synthesis of few-layer MoS₂ nanosheet-coated TiO₂ nanobelts heterostructures for enhanced photocatalytic activities, *Small* 9 (2012) 140–147.
- [46] D.R. Dreyer, S. Park, C.W. Bielański, R.S. Ruoff, The chemistry of graphene oxide, *Chem. Soc. Rev.* 39 (2010) 228–240.
- [47] A. Wu, S. Shen, X. Yan, G. Xia, Y. Zhang, F. Zhu, J. Zhang, C_xN_y particles@N-doped porous graphene: a novel cathode catalyst with a remarkable cyclability for Li-O₂ batteries, *Nanoscale* 10 (2018) 12763–12770.
- [48] G. Wu, N.H. Mack, W. Gao, S. Ma, R. Zhong, J. Han, J.K. Baldwin, P. Zelenay, Nitrogen-doped graphene-rich catalysts derived from heteroatom polymers for oxygen reduction in nonaqueous lithium-O₂ battery cathodes, *ACS Nano* 6 (2012) 9764–9776.
- [49] W. Ma, R. Ma, C. Wang, J. Liang, X. Liu, K. Zhou, T. Sasaki, A superlattice of alternately stacked Ni-Fe hydroxide nanosheets and graphene for efficient splitting of water, *ACS Nano* 9 (2015) 1977–1984.
- [50] W. Cui, Q. Liu, Z. Xing, A.M. Asiri, K.A. Alamry, X. Sun, MoP nanosheets supported on biomass-derived carbon flake: One-step facile preparation and application as a novel high-active electrocatalyst toward hydrogen evolution reaction, *Appl. Catal. B* 164 (2015) 144–150.
- [51] Y. Lin, Y. Pan, J. Zhang, CoP nanorods decorated biomass derived N, P co-doped carbon flakes as an efficient hybrid catalyst for electrochemical hydrogen evolution, *Electrochim. Acta* 232 (2017) 561–569.
- [52] Z. Huang, Z. Chen, Z. Chen, C. Lv, M.G. Humphrey, C. Zhang, Cobalt phosphide nanorods as an efficient electrocatalyst for the hydrogen evolution reaction, *Nano Energy* 9 (2014) 373–382.
- [53] Y. Li, S. Zheng, X. Liu, P. Li, L. Sun, R. Yang, S. Wang, Z. Wu, X. Bao, W. Deng, Conductive microporous covalent triazine-based framework for high-performance electrochemical capacitive energy storage, *Angew. Chem. Int. Ed.* 130 (2017) 8124–8128.
- [54] R. Zhao, M. Wang, D. Zhao, H. Li, C. Wang, L. Yin, Molecular-level heterostructures assembled from titanium carbide MXene and Ni-Co-Al layered double-hydroxide nanosheets for all-solid-state flexible asymmetric high-energy supercapacitors, *ACS Energy Lett.* 3 (2018) 132–140.
- [55] H. Jiang, Y. Liu, W. Li, J. Li, Co nanoparticles confined in 3D nitrogen-doped porous carbon foams as bifunctional electrocatalysts for long-life rechargeable Zn-air batteries, *Small* 14 (2018) 1703739.
- [56] J. Yin, Y. Li, F. Lv, M. Lu, K. Sun, W. Wang, L. Wang, F. Cheng, Y. Li, P. Xi, S. Guo, Oxygen vacancies dominated NiS₂/CoS₂ interface porous nanowires for portable Zn-air batteries driven water splitting devices, *Adv. Mater.* 29 (2017) 1704681.